J. Fluid Mech. (2006), *vol.* 547, *pp.* 185–214. © 2006 Cambridge University Press
doi:10.1017/S0022112005007214 Printed in the United Kingdom

Transverse flows in rapidly oscillating elastic cylindrical shells

By MATTHIAS HEIL[1] AND SARAH L. WATERS[2]

[1]School of Mathematics, University of Manchester, Oxford Road, Manchester M13 9PL, UK
[2]Division of Applied Mathematics, School of Mathematical Sciences, University of Nottingham, University Park, Nottingham, NG7 2RD, UK

(Received 7 October 2004 and in revised form 13 July 2005)

We analyse the flows in fluid-conveying tubes whose elastic walls perform small-amplitude high-frequency oscillations. We show that the velocity perturbations induced by the wall motion are dominated by their transverse components and use numerical simulations to analyse the two-dimensional flows that develop in the tube's cross-sections. Asymptotic methods are then employed to derive explicit predictions for the flow fields and for the total viscous dissipation, whose magnitude plays an important role in the development of self-excited oscillations.

We show that in cases with fluid–structure interaction, the coupled oscillations are controlled by the ratio of the fluid and wall densities, and by a material parameter that is equivalent to the Womersley number, and indicates the importance of fluid inertia and wall elasticity relative to the fluid's viscosity. We present numerical simulations of the coupled oscillations and use asymptotic techniques to derive explicit predictions for their period and decay rate. Finally, we discuss the implications of our results for the development of self-excited oscillations in three-dimensional collapsible tubes.

1. Introduction

Many physiological flows (e.g. blood flow in the veins and arteries or the flow of air in the pulmonary airways) are strongly affected by the interaction between the fluid flow and the vessel wall elasticity. The problem of flow in collapsible tubes has therefore received much interest in the biofluids research community (see, e.g. Heil & Jensen 2003 for a review). Experimentally, the problem is typically studied with a 'Starling resistor', a device in which fluid is driven through a finite-length thin-walled elastic tube which is mounted on two rigid tubes and enclosed in a pressure chamber. One of the most striking features of this system is its propensity to develop large-amplitude self-excited oscillations (see Bertram 2003). Owing to the complexity of the system (an unsteady finite-Reynolds-number flow, interacting with the large displacements of a non-axisymmetrically buckling cylindrical shell), our understanding of the mechanism(s) that initiate and maintain these oscillations is still limited.

In a study of the corresponding two-dimensional model problem (high-Reynolds-number flow through a channel in which part of one wall is replaced by a highly pre-stressed elastic membrane), Jensen & Heil (2003) provided a rational asymptotic description of an instability that causes the development of high-frequency oscillations. The asymptotic predictions were confirmed by direct numerical simulations which showed that the mechanism that is responsible for the initial instability also controls the large-amplitude oscillations that develop subsequently. At leading order, the flow

https://doi.org/10.1017/S0022112005007214 Published online by Cambridge University Press

consists of an inviscid core flow, which represents the axial 'sloshing' of the fluid that is displaced by the transversely oscillating membrane. Thin Stokes layers form on the channel walls. A key ingredient for the instability mechanism is the fact that the inviscid core flow can create a net influx of (kinetic) energy into the system. The development of an instability depends crucially on the ratio of this influx of energy to the viscous dissipation in the Stokes layers.

The ultimate aim of the present study is to investigate how (and if) Jensen & Heil's (2003) two-dimensional instability mechanism can be adjusted to explain the experimentally observed instabilities in three dimensions. While the main ingredients of the instability mechanism are independent of the spatial dimension, there are some important differences between the two-dimensional and three-dimensional systems. In particular, slight buckling of a cylindrical tube only causes small changes in its volume. Therefore, at small buckling amplitudes, the wall deformation only induces small axial flows – the dominant flows occur in the transverse cross-sections. The analysis of these transverse flows is the main subject of this paper.

The outline of our paper is as follows. In § 2, we present the equations that govern three-dimensional unsteady finite-Reynolds-number flows in thin-walled elastic tubes. In § 3, we introduce scaled versions of these equations which are appropriate for the case in which the wall performs small-amplitude high-frequency oscillations. The scaled equations allow the identification of a distinguished parameter regime in which the leading-order oscillatory flow uncouples from the steady through-flow. We then show that for wall deformations that are representative of those encountered in oscillating, thin-walled elastic tubes, the axial component of the unsteady flow that is generated by the wall motion is much smaller than its transverse components. Motivated by this observation, we employ numerical and asymptotic methods to analyse the two-dimensional flows that develop in the tube's transverse cross-sections – initially for the case of prescribed wall motion. In § 4, we extend the analysis to the case with fluid-structure interaction. We present the results of numerical simulations of the coupled oscillations and use asymptotic methods to derive explicit predictions for their period and decay rate. Finally, in § 5 we discuss the implications of our results for the development of self-excited oscillations in three-dimensional collapsible tubes.

2. The problem

We consider the flow of a viscous fluid (density ρ_f and viscosity μ) through an elastic circular cylindrical tube of undeformed radius a and length L whose walls perform flow-induced oscillations. We assume that the flow is driven by a constant pressure drop which is applied between the clamped upstream and downstream ends of the tube. In the absence of any oscillations, this pressure drop would drive a steady flow whose mean velocity we denote by U. The unsteady flow that occurs during the self-excited oscillations is governed by the three-dimensional Navier–Stokes equations

$$\rho_f\left(\frac{\partial \boldsymbol{u}^*}{\partial t^*} + \boldsymbol{u}^*\cdot\nabla\boldsymbol{u}^*\right) = -\nabla p^* + \mu\nabla^2\boldsymbol{u}^*,$$
$$\nabla\cdot\boldsymbol{u}^* = 0. \tag{2.1}$$

(Throughout this paper, asterisks are used to distinguish dimensional quantities from their non-dimensional equivalents.) We parameterize the undeformed wall shape by two Lagrangian coordinates $\xi^{*\alpha}(\alpha = 1, 2)$ as

$$\boldsymbol{r}_w^* = (a\cos(\xi^{*2}/a), a\sin(\xi^{*2}/a), \xi^{*1})^T, \tag{2.2}$$

https://doi.org/10.1017/S0022112005007214 Published online by Cambridge University Press

where $\xi^{*1} \in [0, L]$ and $\xi^{*2} \in [0, 2\pi a]$. The wall is exposed to an external pressure p^*_{ext} and to the fluid traction so that the Cartesian components of the load vector $\boldsymbol{f}^*$ that acts on the wall are given by

$$f_i^* = (p^*_{ext} - p^*)n_i + \mu\left(\frac{\partial u_i^*}{\partial x_j^*} + \frac{\partial u_j^*}{\partial x_i^*}\right)n_j, \tag{2.3}$$

where the x_i^* are Cartesian coordinates and the n_i are the Cartesian components of the inner unit normal $\boldsymbol{n}$ on the wall. Throughout this paper, the summation convention is used and Latin and Greek indices range from 1 to 3 and 1 to 2, respectively. The wall deforms in response to the applied traction, causing the displacement of material particles from their original positions $\boldsymbol{r}^*_w(\xi^{*\alpha})$ to new positions $\boldsymbol{R}^*_w(\xi^{*\alpha}, t^*) = \boldsymbol{r}^*_w(\xi^{*\alpha}) + \boldsymbol{v}^*(\xi^{*\alpha}, t^*)$. The buckling of thin-walled cylindrical shells only induces small strains, therefore we assume linear elastic behaviour (Hooke's law with Young's modulus E and Poisson ratio ν) and describe the deformation of the tube wall by the principle of virtual displacements

$$\int_0^{2\pi a}\int_0^{L}\left[hE^{*\alpha\beta\gamma\delta}\left(\gamma_{\alpha\beta}\delta\gamma_{\gamma\delta} + \tfrac{1}{12}h^2\kappa^*_{\alpha\beta}\delta\kappa^*_{\gamma\delta}\right) - \left(\boldsymbol{f}^* - \rho_w h\frac{\partial^2\boldsymbol{R}^*_w}{\partial t^{*2}}\right)\cdot\delta\boldsymbol{R}^*_w\right]\mathrm{d}\xi^{*1}\,\mathrm{d}\xi^{*2} = 0, \tag{2.4}$$

where

$$E^{*\alpha\beta\gamma\delta} = \frac{E}{2(1+\nu)}\left(\delta^{\alpha\delta}\delta^{\beta\gamma} + \delta^{\alpha\gamma}\delta^{\beta\delta} + \frac{2\nu}{1-\nu}\delta^{\alpha\beta}\delta^{\gamma\delta}\right) \tag{2.5}$$

is the plane-stress stiffness tensor, h the wall thickness, ρ_w the wall density, and $\gamma_{\alpha\beta}$ and $\kappa^*_{\alpha\beta}$ are the midplane strain and bending tensors, respectively (see Wempner 1981 and Appendix A). Finally, the no-slip condition requires that

$$\boldsymbol{u}^* = \frac{\partial\boldsymbol{R}^*_w}{\partial t^*} \quad \text{on the elastic walls.} \tag{2.6}$$

We wish to analyse the fluid–structure interaction problem described by (2.1)–(2.6) in a regime in which the wall performs small-amplitude high-frequency oscillations.

3. Analysis of the flow field for prescribed wall motion

In order to elucidate the characteristic features of the fluid flow, we first consider the case without fluid-structure interaction and assume that the wall performs a prescribed high-frequency harmonic oscillation with period $\mathscr{T}^*$ and amplitude ϵ^*. We will show that the resulting flow is dominated by its transverse velocity components and, using a combination of numerical and asymptotic methods, analyse the two-dimensional flows that develop in the tube's cross-sections.

3.1. *Scaling*

We non-dimensionalize all lengths with the tube radius a and scale the wall displacement $\boldsymbol{v}^*$ on the amplitude of the prescribed wall oscillation, $\epsilon^* = \epsilon a$, where $\epsilon \ll 1$. The tube's undeformed cross-sectional area is then given by $A_{undef} = A^*_{undef}/a^2 = \pi$. We non-dimensionalize time on a time scale T, so that $t^* = Tt$. The deformed wall shape is then given by

$$\boldsymbol{R}_w(\xi^1, \xi^2, t) = (\cos(\xi^2), \sin(\xi^2), \xi^1)^T + \epsilon\boldsymbol{v}(\xi^1, \xi^2, t). \tag{3.1}$$

For the case without fluid–structure interaction, we identify the time scale T with the (known) period of the oscillation, $\mathscr{T}^*$. The prescribed wall displacement $\boldsymbol{v}(\xi^1, \xi^2, t)$

https://doi.org/10.1017/S0022112005007214 Published online by Cambridge University Press

therefore has a harmonic time-dependence with unit period. In § 4 below, where we include fluid–structure interaction, it will be important to distinguish between the time scale T used in the non-dimensionalization of the equations, and the actual (and *a priori* unknown) period $\mathscr{T}^* = T\mathscr{T}$ of the coupled oscillations. To facilitate the transfer of the results, we define

$$\Omega = 2\pi \frac{T}{\mathscr{T}^*} = \frac{2\pi}{\mathscr{T}} \tag{3.2}$$

and take $\Omega \equiv 2\pi$ throughout § 3.

We use $\widehat{U} = a/T$ to non-dimensionalize the velocity and scale the pressure on the associated inertial scale, $\rho_f \widehat{U}^2$. This transforms (2.1) into

$$\frac{\partial \boldsymbol{u}}{\partial t} + \boldsymbol{u}\cdot\nabla\boldsymbol{u} = -\nabla p + \frac{1}{\alpha^2}\nabla^2\boldsymbol{u}, \quad \nabla\cdot\boldsymbol{u} = 0, \tag{3.3}$$

where $\alpha^2 = \rho_f a^2/(\mu T) \gg 1$ is the Womersley number. For the prescribed wall motion considered here, α^2 represents the ratio of the time scale for the diffusion of vorticity across the tube to the period of the oscillation. The no-slip condition (2.6) becomes

$$\boldsymbol{u} = \epsilon\,\partial\boldsymbol{v}/\partial t \quad \text{on the wall}, \tag{3.4}$$

indicating that the wall motion induces unsteady flows of size ϵ.

Alternatively, we can decompose the velocity and pressure fields into their steady and unsteady components,

$$\boldsymbol{u}^* = \overline{\boldsymbol{u}}^*(x_j^*) + \widehat{\boldsymbol{u}}^*(x_j^*, t^*), \quad p^* = \overline{p}^*(x_j^*) + \widehat{p}^*(x_j^*, t^*), \tag{3.5}$$

where the unsteady velocity and pressure fields are assumed to have zero time-average. We non-dimensionalize the steady velocity with the mean axial velocity, $\overline{\boldsymbol{u}}^* = U\overline{\boldsymbol{u}}$, and the unsteady velocity with the wall velocity, $\widehat{\boldsymbol{u}}^* = \epsilon^*/T\,\widehat{\boldsymbol{u}}$. Similarly, pressures are non-dimensionalized as

$$\overline{p}^* = \rho_f U^2 \overline{p}, \quad \widehat{p}^* = \rho_f \frac{\epsilon^* a}{T^2}\widehat{p}. \tag{3.6}$$

The ratio of the size of the unsteady flow induced by the wall motion, ϵ^*/T, to the mean axial velocity, U, is ϵSt where

$$St = \frac{a}{UT} \tag{3.7}$$

is the Strouhal number. In the analysis that follows we consider a regime in which $\epsilon St = \lambda = O(1)$ (so that $St \gg 1$), indicating that the size of the flow induced by the wall motion is comparable to the steady velocities. Equations (2.1) then transform into

$$\frac{\partial \widehat{\boldsymbol{u}}}{\partial t} + \epsilon\lambda\left(\frac{1}{\lambda}\overline{\boldsymbol{u}} + \widehat{\boldsymbol{u}}\right)\cdot\nabla\left(\frac{1}{\lambda}\overline{\boldsymbol{u}} + \widehat{\boldsymbol{u}}\right) = -\nabla\left(\frac{\epsilon}{\lambda^2}\overline{p} + \widehat{p}\right) + \frac{1}{\alpha^2}\nabla^2\left(\frac{1}{\lambda}\overline{\boldsymbol{u}} + \widehat{\boldsymbol{u}}\right) \tag{3.8}$$

$$\nabla\cdot\left(\frac{1}{\lambda}\overline{\boldsymbol{u}} + \widehat{\boldsymbol{u}}\right) = 0, \tag{3.9}$$

subject to

$$\frac{1}{\lambda}\overline{\boldsymbol{u}} + \widehat{\boldsymbol{u}} = \frac{\partial \boldsymbol{v}}{\partial t} \quad \text{on the wall}. \tag{3.10}$$

In addition to λ, the flow is characterized by two dimensionless parameters, $\epsilon \ll 1$ and $\alpha \gg 1$. Since oscillations in collapsible tubes typically develop at large Reynolds number, $Re = a\rho_f U/\mu = \alpha^2/St = O(\epsilon\alpha^2)$, we require that $\alpha^2 \gg 1/\epsilon$.

https://doi.org/10.1017/S0022112005007214 Published online by Cambridge University Press

We now expand all quantities in powers of $\epsilon \ll 1$,

$$\widehat{\boldsymbol{u}}(x_j,t) = \widehat{\boldsymbol{u}}_0(x_j,t) + \epsilon\widehat{\boldsymbol{u}}_1(x_j,t) + \cdots, \quad \widehat{p}(x_j,t) = \widehat{p}_0(x_j,t) + \epsilon\widehat{p}_1(x_j,t) + \cdots,$$
$$\overline{\boldsymbol{u}}(x_j) = \overline{\boldsymbol{u}}_0(x_j) + \epsilon\overline{\boldsymbol{u}}_1(x_j) + \cdots, \quad \overline{p}(x_j) = \overline{p}_0(x_j) + \epsilon\overline{p}_1(x_j) + \cdots.$$

Inserting these expansions into (3.8)–(3.10), expanding in powers of ϵ, and exploiting the fact that all unsteady components have zero time-average, we find that the leading-order unsteady flow $(\widehat{\boldsymbol{u}}_0, \widehat{p}_0)$ is governed by

$$\frac{\partial\widehat{\boldsymbol{u}}_0}{\partial t} = -\nabla\widehat{p}_0 + \frac{1}{\alpha^2}\nabla^2\widehat{\boldsymbol{u}}_0, \quad \nabla\cdot\widehat{\boldsymbol{u}}_0 = 0, \tag{3.11}$$

subject to

$$\widehat{\boldsymbol{u}}_0 = \frac{\partial\boldsymbol{v}}{\partial t} \quad \text{on the wall.} \tag{3.12}$$

Our assumption that $\alpha^2 \gg 1$ implies that in the core region, away from the tube walls, the viscous terms in (3.11) can be neglected so that the flow is governed by the inviscid equations $\partial\widehat{\boldsymbol{u}}_0/\partial t = -\nabla\widehat{p}_0$. Since inviscid flows cannot satisfy the tangential components of the no-slip condition (3.12), we expect the development of Stokes (boundary) layers of thickness $\delta \propto \alpha^{-1}$ on the tube walls. Within these layers, the viscous terms have a size of $O(1)$, justifying their retention in (3.11).

3.2. *The two-dimensional problem for the transverse flows*

To make further progress, we must specify the wall displacement field. Since we wish initially to ignore the fluid–structure interaction, we assume that the wall performs free (*in vacuo*) oscillations about its undeformed shape in one of its eigenmodes. The time-dependent wall displacement field defined in (3.1) is then given by

$$\boldsymbol{v}(\xi^1,\xi^2,t) = \boldsymbol{V}_N(\xi^1,\xi^2)\sin(\Omega t), \tag{3.13}$$

where

$$\boldsymbol{V}_N(\xi^1,\xi^2) = \mathscr{A}(\xi^1)\begin{pmatrix}\cos(N\xi^2)\cos(\xi^2) - \mathbb{A}(\xi^1)\sin(N\xi^2)\sin(\xi^2)\\ \cos(N\xi^2)\sin(\xi^2) + \mathbb{A}(\xi^1)\sin(N\xi^2)\cos(\xi^2)\\ \mathbb{B}(\xi^1)\cos(N\xi^2)\end{pmatrix}. \tag{3.14}$$

Here, N represents the mode's azimuthal wavenumber, and $\mathscr{A}(\xi^1) = O(1)$ is the (normalized) mode shape of the radial wall displacement. The functions $\mathscr{A}(\xi^1)\mathbb{A}(\xi^1)$ and $\mathscr{A}(\xi^1)\mathbb{B}(\xi^1)$ represent the mode shapes of the azimuthal and axial wall displacements, respectively (see, e.g. Soedel 1993).

We now make three observations:

(i) If the displacement field (3.14) is to be representative of the wall deflections that are typically observed during collapsible tube oscillations, $\boldsymbol{V}_N$ should be dominated by its transverse components, implying that $|\mathbb{B}_N(\xi^1)| \ll 1$. In this case, the no-slip condition (3.12) implies that, at least near the wall, the axial component, $\widehat{w}_0$, of the unsteady velocity $\widehat{\boldsymbol{u}}_0$ is much smaller than its transverse components, $\widehat{u}_0$ and $\widehat{v}_0$.

(ii) The change in the tube's cross-sectional area, induced by the wall displacement field (3.13), is a second-order effect, i.e.

$$\frac{\mathrm{d}A(x_3,t)}{\mathrm{d}t} = -\oint_{\partial A}\frac{\partial\boldsymbol{R}_w}{\partial t}\cdot\boldsymbol{n}_\perp\,\mathrm{d}s = O(\epsilon^2), \tag{3.15}$$

where $\boldsymbol{n}_\perp$ is the inner unit normal on a two-dimensional cross-section through the tube, in the plane $x_3 = \text{const}$. From (3.1) and the no-slip condition (3.12), we have

https://doi.org/10.1017/S0022112005007214 Published online by Cambridge University Press

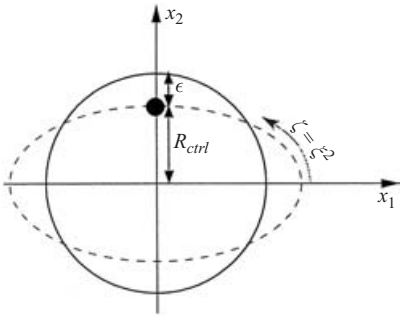


FIGURE 1. Sketch of the two-dimensional problem for the transverse flows. The tube wall performs a high-frequency oscillation of amplitude ϵ and induces an oscillatory flow. The radius R_{ctrl} of the control point on the wall is used to characterize the wall deformation. The Lagrangian coordinate $\zeta = \xi^2$ is used to parameterize the wall shape. The sketch illustrates the wall deformation for the $N = 2$ mode.

$\widehat{\boldsymbol{u}}_0 = \partial \boldsymbol{v}/\partial t = \epsilon^{-1} \partial \boldsymbol{R}_w/\partial t$, therefore

$$-\oint_{\partial A} \frac{\partial \boldsymbol{R}_w}{\partial t} \cdot \boldsymbol{n}_\perp \, \mathrm{d}s = \epsilon \int \left(\frac{\partial \widehat{u}_0}{\partial x_1} + \frac{\partial \widehat{v}_0}{\partial x_2} \right) \mathrm{d}A = -\epsilon \int \frac{\partial \widehat{w}_0}{\partial x_3} \, \mathrm{d}A = O(\epsilon^2), \tag{3.16}$$

where we have used the two-dimensional divergence theorem and the incompressibility condition (3.11*b*). This shows that the cross-sectional average of $\partial \widehat{w}_0/\partial x_3$ has size $O(\epsilon)$. Furthermore, over a non-dimensional tube length of L/a, the oscillatory wall motion generates axial flows whose cross-sectional average has size $O(\epsilon L/a)$. If $\epsilon L/a \ll 1$, the cross-sectional average of $\widehat{w}_0$ is much smaller than the transverse velocity components $\widehat{u}_0$ and $\widehat{v}_0$.

(iii) Under the long-wavelength assumption $L/a \gg 1$, the three-dimensional Laplace operator in (3.11) can be approximated by its two-dimensional equivalent $\nabla_\perp^2 = \partial^2/\partial x_1^2 + \partial^2/\partial x_2^2$.

Observations (i) and (ii) suggest that $|\widehat{w}_0| \ll 1$ throughout the domain, implying that the unsteady velocity $\widehat{\boldsymbol{u}}_0$ is dominated by its transverse components. We adopt this plausible assumption by setting $\widehat{w}_0 \equiv 0$ and, based on observation (iii), neglect the axial derivatives in equations (3.11) and (3.12). The leading-order oscillatory flow $(\widehat{u}_0, \widehat{v}_0, \widehat{p}_0)$ is then two-dimensional and can be determined independently in each cross-section by solving the two-dimensional problem sketched in figure 1. Fluid is enclosed by an oscillating wall whose time-dependent shape is parameterized by the single Lagrangian coordinate $\zeta = \xi^2$ as

$$\boldsymbol{R}_w(\zeta, t) = R_0 \begin{pmatrix} \cos(\zeta) \\ \sin(\zeta) \end{pmatrix} + \epsilon \boldsymbol{V}_N(\zeta) \sin(\Omega t), \tag{3.17}$$

with

$$\boldsymbol{V}_N(\zeta) = \mathscr{A} \begin{pmatrix} \cos(N\zeta)\cos(\zeta) - \mathbb{A} \sin(N\zeta)\sin(\zeta) \\ \cos(N\zeta)\sin(\zeta) + \mathbb{A} \sin(N\zeta)\cos(\zeta) \end{pmatrix}, \tag{3.18}$$

where $\mathbb{A}$ is the ratio of the azimuthal and radial displacement amplitudes. The $O(1)$ parameter R_0 is introduced to facilitate the numerical simulations discussed in § 3.4.1; elsewhere we set $R_0 \equiv 1$.

3.3. *The hierarchy of scales*

The governing equations (3.11) and (3.12) contain only a single dimensionless parameter, α. In §§ 3.4.2 and 4.2.2, we will perform an asymptotic analysis of the

https://doi.org/10.1017/S0022112005007214 Published online by Cambridge University Press

two-dimensional problem, exploiting the fact that $\alpha \gg 1$. We will expand the dependent variables $(\widehat{\boldsymbol{u}}_0, \widehat{p}_0)$ in powers of $1/\alpha$, retaining terms of size $O(1/\alpha)$. This is, of course, only consistent if the errors introduced during the derivation of the two-dimensional problem are of size $O(1/\alpha)$. This imposes constraints on the relative sizes of the parameters. α, ϵ and L/a.

(i) In the derivation of the three-dimensional equations (3.11) and (3.12) from (3.8) and (3.10), we neglected terms of size $O(\epsilon)$. Consistency therefore requires that $\epsilon \ll 1/\alpha$.

(ii) In § 3.2, we employed the assumptions $|\mathbb{B}(\xi^1)| \ll 1$ and $\epsilon L/a \ll 1$ to neglect the axial velocities. To make this consistent with the subsequent expansions in $1/\alpha$, we make these bounds more specific by assuming that $|\mathbb{B}(\xi^1)| \ll 1/\alpha$ and $\epsilon L/a \ll 1/\alpha$.

(iii) The long-wavelength assumption, $L/a \gg 1$, which allowed us to replace the three-dimensional Laplace operator by its two-dimensional equivalent, $\nabla^2_\perp$, introduces an error of size $O((L/a)^{-2})$. Consistency therefore requires that $L/a \gg \alpha^{1/2}$.

The last two conditions impose the constraints

$$\alpha^{1/2} \ll \frac{L}{a} \ll \frac{1}{\alpha\epsilon}, \tag{3.19}$$

where consistency between the upper and lower bounds requires that $1/\epsilon \gg \alpha^{3/2}$. We have already assumed that $\alpha^2 \gg 1/\epsilon$ to reflect the large Reynolds number of the mean flow. To formally justify the asymptotic expansions in §§ 3.4.2 and 4.2.2 we therefore assume that α and ϵ satisfy the constraints

$$\alpha^2 \gg \frac{1}{\epsilon} \gg \alpha^{3/2} [\gg \alpha] \gg 1. \tag{3.20}$$

3.4. *Analysis of the transverse flows*

3.4.1. *Numerical simulations*

We will first use numerical simulations to explore the two-dimensional flows that are generated by the oscillating wall. We employed Heil & Hazel's (2005) fully adaptive object-oriented finite-element library `oomph-lib` to solve the arbitrary Lagrangian Eulerian formulation of the Navier–Stokes equations (3.3) in the two-dimensional domain bounded by (3.17), subject to the no-slip boundary conditions (3.4). In most collapsible-tube experiments, the wall deforms in its $N = 2$ mode, therefore we only considered the flow in the quarter domain $x_1, x_2 \geqslant 0$ and applied symmetry conditions along the coordinate axes (see Appendix C for a more detailed discussion of this symmetry assumption). The equations were discretized with LBB-stable quadrilateral `Q2Q-1` elements and time-stepping was performed with the BDF4 scheme with fixed time step. Unstructured quadtree mesh refinement procedures, based on Z2 error estimation (Zienkiewicz & Zhu 1992), were employed to resolve the thin Stokes layers that develop near the wall. Newton's method was employed to solve the large system of nonlinear algebraic equations that arise at every time step; the linear systems were assembled and LU-decomposed by the frontal solver MA42 from the HSL2000 library.

As discussed in § 3.2, the change in cross-sectional area induced by the displacement field (3.17) is of order $O(\epsilon^2)$ and hence very small. Nevertheless, the displacement field violates the exact mass conservation required by (3.3). In the computations, we therefore treated R_0 as a variable and determined its value as part of the solution. This was achieved by making R_0 a linear function of the fluid pressure at a fixed point which we chose to be the origin. This allows the wall to stretch and contract as required to satisfy global mass conservation. As expected, we observed that $|R_0(t) - 1| \ll 1$ throughout the simulation; see Appendix B for further details.

https://doi.org/10.1017/S0022112005007214 Published online by Cambridge University Press

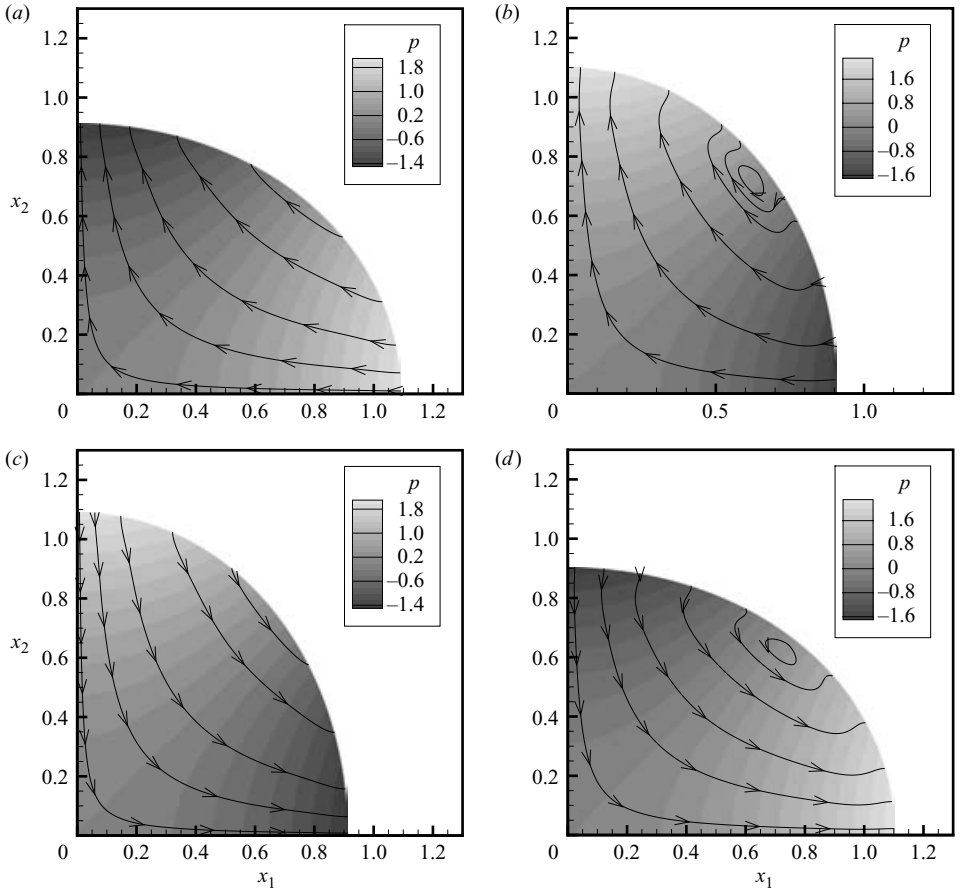


FIGURE 2. Streamlines and pressure contours during four instants of the oscillation. $\alpha^2 = 100$, $\epsilon = 0.1$; wall motion given by (3.17) with $N = 2$ and $\mathbb{A} = -0.5$. (*a*) $t = 0.325$, (*b*) $t = 0.725$, (*c*) $t = 0.825$, (*d*) $t = 1.225$. Only one quarter of the domain is shown.

Figure 2 shows the results from the direct numerical simulations for $\alpha^2 = 100$. The wall performs oscillations of amplitude $\epsilon = 0.1$ in its $N = 2$ mode with an amplitude ratio of $\mathbb{A} = -0.5$ which is appropriate for thin-walled elastic rings that perform *in vacuo* oscillations in their bending mode (see Soedel 1993 and § 4.2.2). The figure shows the instantaneous streamlines and pressure contours during four characteristic phases of the oscillation. In figure 2(*a*), the wall accelerates towards its undeformed configuration and the flow is driven by a strong 'favourable' pressure gradient. The core flow resembles an unsteady stagnation-point flow; thin boundary layers develop near the wall, but they play a purely passive role and have little effect on the overall flow field. In figure 2(*b*), the wall decelerates as it approaches the most strongly deformed configuration. The fluid is now decelerated by a strong 'adverse' pressure gradient which appears to cause large-scale flow separation and leads to the formation of a large vortex near the wall. Figures 2(*c*) and 2(*d*) display the flow during the second half of the cycle, when the direction of the motion is reversed.

The surface plot of the velocities, shown in figure 3, provides a clearer illustration of the flow structure. There is a large core region in which the flow has the character

https://doi.org/10.1017/S0022112005007214 Published online by Cambridge University Press

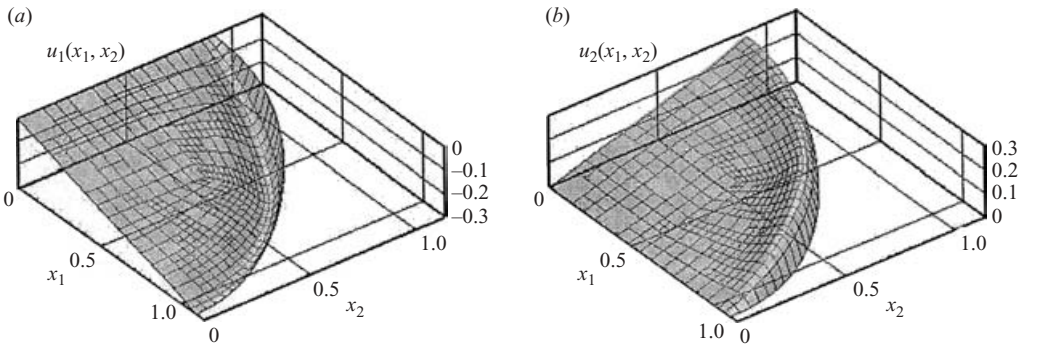


FIGURE 3. Plot of the two Cartesian velocity components $u_i(x_1, x_2)$ for $i = 1, 2$ at $t = 0.325$. $\alpha^2 = 100, \epsilon = 0.1$; wall motion given by (3.17) with $N = 2$ and $\mathbb{A} = -0.5$. Only one quarter of the domain is shown. Wire-mesh plot: finite-element results; shaded surface: compound asymptotics (3.39).

of an unsteady stagnation, point flow ($u_1 \propto -x_1, u_2 \propto x_2$); this inviscid flow region is matched to the moving wall with boundary layers of thickness $\delta \approx \alpha^{-1} = 0.1$.

An inspection of the instantaneous spatial distribution of the non-dimensional viscous dissipation

$$d = \frac{d^*}{\mu/T^2} = 2\left(e_{11}^2 + 2e_{12}^2 + e_{22}^2\right), \tag{3.21}$$

where e_{ij} is the rate-of-strain tensor, $e_{ij} = T e_{ij}^* = (\partial u_i/\partial x_j + \partial u_j/\partial x_i)/2$ shows that the dissipation is spatially uniform and relatively small in the core region and strongly elevated in the boundary layer. This suggests that the total dissipation

$$D = \frac{D^*}{\mu(a/T)^2} = \int d \, \mathrm{d}A \tag{3.22}$$

should be dominated by the contribution from the boundary layer. This allows us to estimate the dependence of D on the problem parameters $\alpha \gg 1$ and $\epsilon \ll 1$ as follows. The boundary-layer thickness δ varies like $\delta \sim \alpha^{-1}$ (see § 3.1), so inside the boundary layer $e_{ij} \sim \delta^{-1} \sim \alpha$. The area occupied by the boundary layer varies like $\delta \sim \alpha^{-1}$, therefore we expect that $D \propto \alpha$. Similarly, since the velocities scale like ϵ (see equation (3.4)), we expect that $D \propto \epsilon^2$. These scalings are partially confirmed by the numerical simulations, as will be demonstrated in § 3.4.3.

3.4.2. *Asymptotic analysis*

The numerical simulations presented in § 3.4.1 confirm the boundary-layer structure of the flow that is suggested by the form of equation (3.11) in the limit of large Womersley number. We now seek asymptotic expressions for the flow quantities. For this purpose, we introduce the transformation

$$\begin{pmatrix} x_1(\rho, \zeta, t) \\ x_2(\rho, \zeta, t) \end{pmatrix} = \rho \boldsymbol{R}_w(\zeta, t), \tag{3.23}$$

to establish a moving body-fitted coordinate system (ρ, ζ). Here, $\zeta \in [0, 2\pi]$ is the Lagrangian coordinate used to parameterize the wall shape in (3.17) and $\rho \in [0, 1]$, so that the wall is located at $\rho = 1$ (see figure 4). We decompose the velocity vector in the direction of the time-dependent unit vectors, $\boldsymbol{e}_\zeta$ and $\boldsymbol{e}_\rho$, tangent to the coordinate

https://doi.org/10.1017/S0022112005007214 Published online by Cambridge University Press

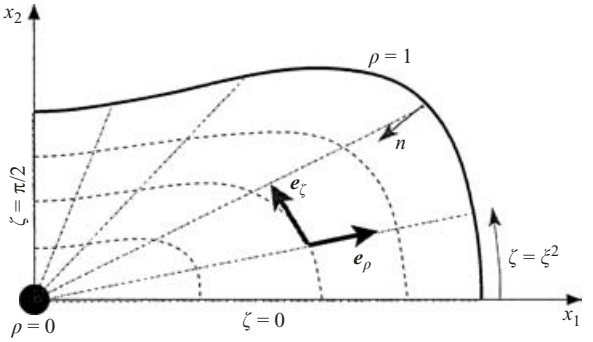


FIGURE 4. Sketch of the body-fitted coordinate system (ρ, ζ) and the boundary-layer coordinate n.

lines, as

$$\widehat{\boldsymbol{u}}_0(\rho, \zeta, t) = \widehat{u}_0^\rho(\rho, \zeta, t)\boldsymbol{e}_\rho(\rho, \zeta, t) + \widehat{u}_0^\zeta(\rho, \zeta, t)\boldsymbol{e}_\zeta(\rho, \zeta, t). \tag{3.24}$$

The components of the wall velocity $\partial \boldsymbol{R}_w(\zeta, t)/\partial t = \epsilon(\widehat{U}_w^\rho(\zeta, t)\boldsymbol{e}_\rho + \widehat{U}_w^\zeta(\zeta, t)\boldsymbol{e}_\zeta)$, relative to this coordinate system, are given by

$$\widehat{U}_w^\rho(\zeta, t) = \mathscr{A}\Omega\cos(N\zeta)\cos(\Omega t), \quad \widehat{U}_w^\zeta(\zeta, t) = \mathscr{A}\mathbb{A}\Omega\sin(N\zeta)\cos(\Omega t). \tag{3.25a, b}$$

Therefore the no-slip condition (3.12) becomes

$$\widehat{u}_0^\rho(\rho = 1, \zeta, t) = \widehat{U}_w^\rho(\zeta, t), \quad \widehat{u}_0^\zeta(\rho = 1, \zeta, t) = \widehat{U}_w^\zeta(\zeta, t). \tag{3.26a, b}$$

We expand the dependent variables in powers of α^{-1} as follows:

$$\widehat{\boldsymbol{u}}_0 = \widehat{\boldsymbol{u}}_{00} + \frac{1}{\alpha}\widehat{\boldsymbol{u}}_{01} + \cdots, \quad \widehat{p}_0 = \widehat{p}_{00} + \frac{1}{\alpha}\widehat{p}_{01} + \cdots. \tag{3.27a, b}$$

Since we expect the development of a Stokes (boundary) layer of thickness $\delta = O(\alpha^{-1})$ near the wall, we expand the variables in the boundary layer as

$$\widehat{u}_0^\rho(n, \zeta, t) = \widehat{U}_w^\rho(\zeta, t) + \frac{1}{\alpha}\widehat{U}_{00}^\rho(n, \zeta, t) + \frac{1}{\alpha^2}\widehat{U}_{01}^\rho(n, \zeta, t) + \cdots, \tag{3.28a}$$

$$\widehat{u}_0^\zeta(n, \zeta, t) = \widehat{U}_{00}^\zeta(n, \zeta, t) + \frac{1}{\alpha}\widehat{U}_{01}^\zeta(n, \zeta, t) + \cdots, \tag{3.28b}$$

$$\widehat{p}_0(n, \zeta, t) = \widehat{P}_{00}(n, \zeta, t) + \frac{1}{\alpha}\widehat{P}_{01}(n, \zeta, t) + \cdots, \tag{3.28c}$$

where $n = \alpha(1 - \rho)$ is the boundary-layer coordinate, measured in the direction of the inner unit normal on the wall, $\boldsymbol{n}_\perp$ (see figure 4).

The core flow solutions are matched to those in the boundary layer by Van Dyke's matching rule (Van Dyke 1964). We expand the core solution about $\rho = 1$ and express the result in terms of the boundary-layer coordinate n. Matching then requires that

$$\lim_{n\to\infty}\left(\widehat{U}_w^\rho + \frac{1}{\alpha}\widehat{U}_{00}^\rho + \cdots\right) = \widehat{u}_{00}^\rho\Big|_{\rho=1} + \frac{1}{\alpha}\left(-n\frac{\partial \widehat{u}_{00}^\rho}{\partial\rho}\Big|_{\rho=1} + \widehat{u}_{01}^\rho\Big|_{\rho=1}\right) + \cdots, \tag{3.29a}$$

$$\lim_{n\to\infty}\left(\widehat{U}_{00}^\zeta + \frac{1}{\alpha}\widehat{U}_{01}^\zeta + \cdots\right) = \widehat{u}_{00}^\zeta\Big|_{\rho=1} + \frac{1}{\alpha}\left(-n\frac{\partial \widehat{u}_{00}^\zeta}{\partial\rho}\Big|_{\rho=1} + \widehat{u}_{01}^\zeta\Big|_{\rho=1}\right) + \cdots, \tag{3.29b}$$

$$\lim_{n\to\infty}\left(\widehat{P}_{00} + \frac{1}{\alpha}\widehat{P}_{01} + \cdots\right) = \widehat{p}_{00}\Big|_{\rho=1} + \frac{1}{\alpha}\left(-n\frac{\partial \widehat{p}_{00}}{\partial\rho}\Big|_{\rho=1} + \widehat{p}_{01}\Big|_{\rho=1}\right) + \cdots. \tag{3.29c}$$

https://doi.org/10.1017/S0022112005007214 Published online by Cambridge University Press

a. The leading-order problem

Substitution of (3.23) and (3.27) into (3.11) shows that the leading-order problem for $(\widehat{\boldsymbol{u}}_{00}, \widehat{p}_{00})$ is given by the inviscid equations

$$\frac{\partial \widehat{\boldsymbol{u}}_{00}}{\partial t} = -\nabla_\perp \widehat{p}_{00}, \quad \nabla_\perp \cdot \widehat{\boldsymbol{u}}_{00} = 0, \text{ where } \nabla_\perp = \left(\frac{\partial}{\partial \rho}, \frac{1}{\rho}\frac{\partial}{\partial \zeta}\right). \tag{3.30}$$

These equations must be solved subject to the matching condition (3.29*a*) whose leading-order contribution requires that $\widehat{u}^\rho_{00} = \widehat{U}^\rho_w$ at $\rho = 1$. We seek a potential flow solution of the form $\widehat{\boldsymbol{u}}_{00} = \nabla_\perp \phi_{00}$. Equation (3.30*b*) then implies $\nabla^2_\perp \phi_{00} = 0$, which must be solved subject to $\partial\phi_{00}/\partial\rho = \widehat{U}^\rho_w$ at $\rho = 1$. The solution is

$$\begin{pmatrix} \widehat{u}^\rho_{00} \\ \widehat{u}^\zeta_{00} \end{pmatrix} = \mathscr{A}\Omega\rho^{N-1}\cos(\Omega t)\begin{pmatrix} \cos(N\zeta) \\ -\sin(N\zeta) \end{pmatrix}, \quad \widehat{p}_{00} = \mathscr{A}\frac{\Omega^2}{N}\rho^N \cos(N\zeta)\sin(\Omega t). \tag{3.31a, b}$$

As expected, the velocity field (3.31*a*) does not satisfy the tangential component of the no-slip condition (3.26*b*) and hence it is necessary to consider the flow in the Stokes layer. The leading-order equations that govern the flow in this layer are

$$\frac{\partial \widehat{U}^\zeta_{00}}{\partial t} = -\frac{\partial \widehat{P}_{00}}{\partial \zeta} + \frac{\partial^2 \widehat{U}^\zeta_{00}}{\partial n^2}, \quad \frac{\partial \widehat{P}_{00}}{\partial n} = 0, \quad \frac{\partial \widehat{U}^\zeta_{00}}{\partial \zeta} - \frac{\partial \widehat{U}^\rho_{00}}{\partial n} + \widehat{U}^\rho_w = 0. \tag{3.32}$$

These equations must be solved subject to the no-slip conditions $\widehat{U}^\rho_{00} = 0$, $\widehat{U}^\zeta_{00} = \widehat{U}^\zeta_w$ at $n = 0$. At leading order, the matching conditions (3.29*b*) and (3.29*c*) require that $\widehat{U}^\zeta_{00} \to -\mathscr{A}\Omega\sin(N\zeta)\cos(\Omega t)$ and $\widehat{P}_{00} \to \mathscr{A}\Omega^2/N\cos(N\zeta)\sin(\Omega t)$ as $n \to \infty$. The solution is

$$\left.\begin{aligned} \widehat{U}^\rho_{00} &= \mathscr{A}\cos(N\zeta)\big[-n\Omega(N-1)\cos(\Omega t) + \sqrt{\Omega}N(1+\mathbb{A}) \\ &\quad \times\big(\sin\left(\Omega t + \tfrac{1}{4}\pi\right) - \mathrm{e}^{-n\sqrt{\Omega/2}}\sin\left(-\sqrt{\tfrac{1}{2}\Omega}n + \Omega t + \tfrac{1}{4}\pi\right)\big)\big], \\ \widehat{U}^\zeta_{00} &= \mathscr{A}\sin(N\zeta)\big[\Omega(1+\mathbb{A})\mathrm{e}^{-n\sqrt{\Omega/2}}\cos\left(-\sqrt{\tfrac{1}{2}\Omega}n + \Omega t\right) - \Omega\cos(\Omega t)\big], \\ \widehat{P}_{00} &= \mathscr{A}\frac{\Omega^2}{N}\cos(N\zeta)\sin(\Omega t). \end{aligned}\right\} \tag{3.33}$$

b. The first-order problem

At $O(\alpha^{-1})$ the governing equations are

$$\frac{\partial \widehat{\boldsymbol{u}}_{01}}{\partial t} = -\nabla_\perp \widehat{p}_{01}, \quad \nabla_\perp \cdot \widehat{\boldsymbol{u}}_{01} = 0, \tag{3.34}$$

which, from the matching condition (3.29*a*), must be solved subject to $\widehat{u}^\rho_{01} = \mathscr{A}\sqrt{\Omega}N(1+\mathbb{A})\cos(N\zeta)\sin(\Omega t + \pi/4)$ at $\rho = 1$. The solution is

$$\left.\begin{aligned} \begin{pmatrix} \widehat{u}^\rho_{01} \\ \widehat{u}^\zeta_{01} \end{pmatrix} &= \mathscr{A}\sqrt{\Omega}N(1+\mathbb{A})\rho^{N-1}\begin{pmatrix} \cos(N\zeta) \\ -\sin(N\zeta) \end{pmatrix}\sin\left(\Omega t + \tfrac{1}{4}\pi\right), \\ \widehat{p}_{01} &= -\mathscr{A}\Omega\sqrt{\Omega}(1+\mathbb{A})\rho^N\cos(N\zeta)\cos\left(\Omega t + \tfrac{1}{4}\pi\right). \end{aligned}\right\} \tag{3.35}$$

Again, the solution (3.35) does not satisfy the tangential component of the no-slip condition (3.26*b*) which requires that $\widehat{u}^\zeta_{01}(\rho = 1, \zeta, t) = 0$. The flow in the Stokes layer is now governed by

$$\frac{\partial \widehat{U}^\zeta_{01}}{\partial t} = -\frac{\partial \widehat{P}_{01}}{\partial \zeta} - n\frac{\partial \widehat{P}_{00}}{\partial \zeta} + \frac{\partial^2 \widehat{U}^\zeta_{01}}{\partial n^2}, \quad \frac{\partial \widehat{U}^\rho_w}{\partial t} = \frac{\partial \widehat{P}_{01}}{\partial n}, \tag{3.36}$$

$$n\widehat{U}^\rho_w + \widehat{U}^\rho_{00} - \frac{\partial \widehat{U}^\rho_{01}}{\partial n} + n\frac{\partial \widehat{U}^\zeta_{00}}{\partial \zeta} + \frac{\partial \widehat{U}^\zeta_{01}}{\partial \zeta} = 0. \tag{3.37}$$

https://doi.org/10.1017/S0022112005007214 Published online by Cambridge University Press

The no-slip conditions are $\widehat{U}_{01}^{\zeta} = 0$ at $n = 0$ and the matching conditions follow from (3.29*b*) and (3.29*c*), but are too lengthy to quote here. The solution is

$$\left.\begin{aligned}\widehat{U}_{01}^{\zeta} &= \mathscr{A}\sin(N\zeta)\big[-n\Omega(1-N)\cos(\Omega t) + \sqrt{\Omega}N(1+\mathbb{A}) \\ &\quad\times\big(\mathrm{e}^{-n\sqrt{\Omega/2}}\sin\big(-\sqrt{\tfrac{1}{2}\Omega}n + \Omega t + \tfrac{1}{4}\pi\big) - \sin\big(\Omega t + \tfrac{1}{4}\pi\big)\big)\big], \\ \widehat{P}_{01} &= -\mathscr{A}\cos(N\zeta)\big[n\Omega^2\sin(\Omega t) + \Omega\sqrt{\Omega}(1+\mathbb{A})\cos\big(\Omega t + \tfrac{1}{4}\pi\big)\big].\end{aligned}\right\} \tag{3.38}$$

The radial velocity component, $\widehat{U}_{01}^{\rho}$, can be obtained from (3.37), but is not required for the first two terms of the expansion (3.27*a*).

c. The composite solution

To facilitate direct comparisons with the numerical solutions, we construct composite expansions that are valid throughout the entire domain. Using standard procedures (see, e.g. Hinch 1991), the expansions for velocity and pressure given in (3.31), (3.33), (3.35) and (3.38) can be combined to the composite approximations

$$\left.\begin{aligned}\widehat{u}_0^{\rho} &= \mathscr{A}\cos(N\zeta)\bigg[\Omega\rho^{N-1}\cos(\Omega t) + \frac{\sqrt{\Omega}N(1+\mathbb{A})}{\alpha}\big(\rho^{N-1}\sin\big(\Omega t + \tfrac{1}{4}\pi\big) \\ &\qquad - \mathrm{e}^{-\sqrt{\Omega/2}\alpha(1-\rho)}\sin\big(-\sqrt{\tfrac{1}{2}\Omega}\alpha(1-\rho) + \Omega t + \tfrac{1}{4}\pi\big)\big)\bigg], \\ \widehat{u}_0^{\zeta} &= \mathscr{A}\sin(N\zeta)\bigg[-\Omega\rho^{N-1}\cos(\Omega t) + \Omega(1+\mathbb{A})\mathrm{e}^{-\sqrt{\Omega/2}\alpha(1-\rho)} \\ &\qquad\times\cos\big(-\sqrt{\tfrac{1}{2}\Omega}\alpha(1-\rho) + \Omega t\big) - \frac{\sqrt{\Omega}N(1+\mathbb{A})}{\alpha} \\ &\qquad\times\big(\rho^{N-1}\sin\big(\Omega t + \tfrac{1}{4}\pi\big) - \sin\big(-\sqrt{\tfrac{1}{2}\Omega}\alpha(1-\rho) + \Omega t + \tfrac{1}{4}\pi\big)\big)\bigg], \\ \widehat{p}_0 &= \mathscr{A}\cos(N\zeta)\rho^N\left[\frac{\Omega^2}{N}\sin(\Omega t) - \frac{1}{\alpha}\Omega\sqrt{\Omega}(1+\mathbb{A})\cos\big(\Omega t + \tfrac{1}{4}\pi\big)\right],\end{aligned}\right\} \tag{3.39}$$

which include all terms up to $O(\alpha^{-1})$.

The instantaneous total dissipation D in the fluid, defined in (3.22), is given by

$$D(t) = \tfrac{1}{8}\epsilon^2\mathscr{A}^2\Omega^2\pi(\alpha\mathscr{D}_0(t) + \mathscr{D}_1(t)) + O(\epsilon^2\alpha^{-1}), \tag{3.40}$$

where

$$\mathscr{D}_0(t) = \alpha\sqrt{2\Omega}(1+\mathbb{A})^2(2 + \cos(2\Omega t) - \sin(2\Omega t)), \tag{3.41}$$

and

$$\mathscr{D}_1(t) = 32(N-1)\cos^2(\Omega t) + (1+\mathbb{A})(-(1+\mathbb{A}) + \cos^2(\Omega t)(-10\mathbb{A} + 8\mathbb{A}N - 24N + 22)), \tag{3.42}$$

while the total energy loss due to dissipation during one period of the oscillation is given (to the same order of accuracy as in (3.40)) by

$$\Pi_{diss} = \int_0^{2\pi/\Omega} D(t)\,\mathrm{d}t = \tfrac{1}{2}\epsilon^2\mathscr{A}^2\Omega\pi^2\big[\alpha\sqrt{2\Omega}(1+\mathbb{A})^2 + \mathbb{A}(\mathbb{A}(2N-3) + 2 - 4N)\big]. \tag{3.43}$$

3.4.3. *Comparison between asymptotics and numerics*

Figure 5 shows the time trace of the total viscous dissipation, $D(t)$, for a small-amplitude wall oscillation ($\epsilon = 0.01$) at a Womersley number of $\alpha^2 = 400$. The total

https://doi.org/10.1017/S0022112005007214 Published online by Cambridge University Press

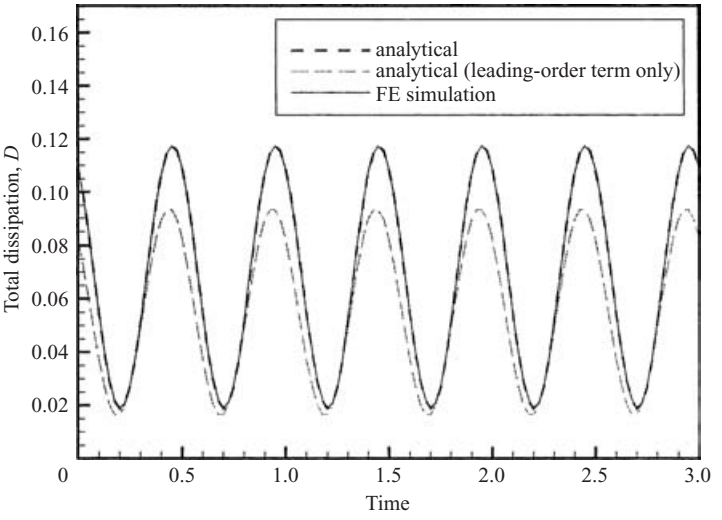


FIGURE 5. Total dissipation $D(t)$ for $\epsilon = 0.01$, $N = 2$, $\mathbb{A} = -0.5$ and $\alpha^2 = 400$. Solid lines: numerical results; broken lines: asymptotic predictions from (3.40).

dissipation varies with twice the frequency of the wall motion and its maxima (minima) occur close to the instants when the wall passes through its undeformed (most strongly deformed) configuration. Because of inertia, fluid does not come to a rest when the wall is in its most strongly deformed configuration. Hence, there is a slight phase shift between the wall motion and the viscous dissipation $D(t)$. Furthermore, $D(t)$ remains non-zero over the entire period of the oscillation. The comparison between the numerical and asymptotic predictions in figure 5 shows that the leading-order approximation $(\Omega^2\pi\epsilon^2\mathscr{A}^2\alpha\mathscr{D}_0(t)/8)$, based on the velocity field $\widehat{\boldsymbol{u}}_{00}$, significantly underestimates the total dissipation. The $O(1)$ correction, associated with $\widehat{\boldsymbol{u}}_{01}$, improves the asymptotic approximation for $D(t)$ considerably and the prediction based on (3.40) is virtually indistinguishable from the numerical results. This shows that, in the parameter regime considered here, the *a priori* estimate $D \sim \alpha$ of § 3.4.1 is inaccurate because the dissipation in the core region cannot be neglected. Figure 6 compares the numerical and asymptotic predictions for $\epsilon = 0.1$ and for a wider range of Womersley numbers. The figure shows that the asymptotic approximation (3.40) still performs extremely well at larger amplitudes and at much smaller Womersley numbers. The numerical simulations confirm the *a priori* estimate $D \sim \epsilon^2$, providing further justification for the linearization of the Navier–Stokes equations (3.3) in (3.11) and (3.12).

Figure 3 demonstrates that the asymptotic theory not only provides excellent predictions for the total dissipation (an integral measure of the solution), but also for the (pointwise) velocities, which agree extremely well with the computed results. The asymptotic solution therefore allows us to analyse the mechanism responsible for the short phase of 'flow separation' that appears to occur towards the end of the deceleration phase (see figure 2*b*, *d*). Equation (3.39*b*) shows that $\partial\widehat{u}_0^{\zeta}/\partial n \sim \sin(N\zeta)$, indicating that the wall shear stress retains the same sign along the entire fraction of the wall shown in figure 2. The large vortex that develops during this phase of the oscillation is, therefore, not associated with flow separation in the sense of classical boundary-layer theory. Furthermore, close inspection of the velocity field shows that the vortex is completely contained inside the boundary layer which, at a Womersley number of $\alpha^2 = 100$, has a thickness of approximately 10 % of the tube

https://doi.org/10.1017/S0022112005007214 Published online by Cambridge University Press

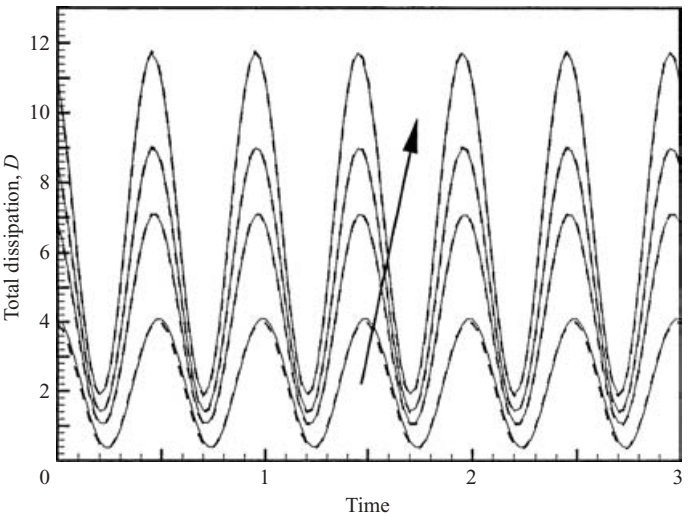


FIGURE 6. Total dissipation $D(t)$ for $\epsilon = 0.1$, $N = 2$ and $\mathbb{A} = -0.5$. Solid lines: numerical results; dashed lines: asymptotic predictions from (3.40). $\alpha^2 = 10, 100, 200, 400$ increasing in the direction of the arrow.

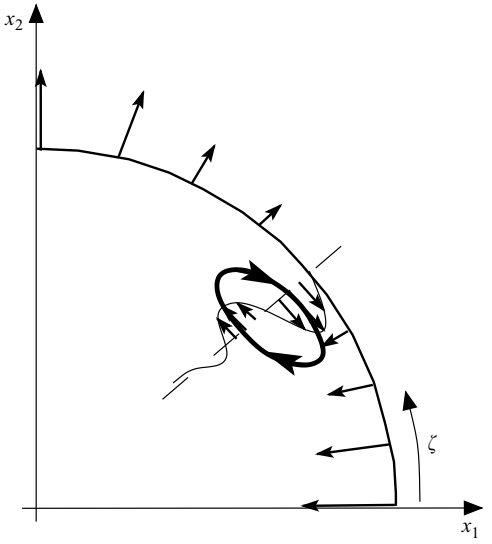


FIGURE 7. Sketch illustrating the generation of a vortex inside the Stokes (boundary) layer.

radius. The analysis of § 3.4.2 shows that the structure of the flow inside the boundary layer is analogous to the flow in the Stokes layer above an oscillating plate: the tangential fluid velocities $\widehat{U}_0^{\zeta}(n, \zeta, t)$ in different tangential 'layers' of the boundary layer are out of phase relative to each other. Furthermore, $\widehat{U}_0^{\zeta}$ decays rapidly with increasing n and periodically changes sign. In the present problem, the azimuthal periodicity of the wall displacement field modulates this tangential boundary-layer velocity profile by $\sin(N\zeta)$, and the wall motion generates a wall-normal velocity component $\widehat{U}_w^{\rho} \sim \cos(N\zeta)$. The resulting flow is sketched in figure 7 which illustrates how this velocity field generates a vortex near the central part of the tube wall.

https://doi.org/10.1017/S0022112005007214 Published online by Cambridge University Press

4. Analysis with fluid–structure interaction

We will now extend the analysis of § 3 to include fluid–structure interaction by allowing the wall to deform in response to the traction that the fluid exerts on it.

4.1. *Non-dimensionalization*

Assuming that the oscillations are governed by a balance between unsteady fluid inertia (which scales like $\rho_f \widehat{U}^2 = \rho_f (a/T)^2$) and wall elasticity (characterized by the wall's bending stiffness $K = (h/a)^3 E/[12(1-\nu^2)]$), the time scale of the oscillations is given by $T = a\sqrt{\rho_f/K}$. Hence, the Womersley number α in (3.3) becomes

$$\alpha = \left(\frac{a}{\mu}\right)^{1/2} (K\rho_f)^{1/4} \tag{4.1}$$

while the Strouhal number is given by

$$St = \frac{1}{U}\left(\frac{K}{\rho_f}\right)^{1/2}. \tag{4.2}$$

We non-dimensionalize the external pressure on the wall's bending stiffness K and use the undeformed tube radius a to non-dimensionalize all lengths. This transforms the variational principle (2.4) into

$$0 = \int\int \left\{ E^{\alpha\beta\gamma\delta}\left(\gamma_{\alpha\beta}\delta\gamma_{\gamma\delta} + \frac{1}{12}\left(\frac{h}{a}\right)^2 \kappa_{\alpha\beta}\delta\kappa_{\gamma\delta}\right) - \frac{(h/a)^3}{12(1-\nu^2)}\left[\left(\frac{a}{h}\right)\boldsymbol{f} - \left(\frac{\rho_w}{\rho_f}\right)\frac{\partial^2 \boldsymbol{R}_w}{\partial t^2}\right]\cdot\delta\boldsymbol{R}_w \right\} \mathrm{d}\xi^1\,\mathrm{d}\xi^2, \tag{4.3}$$

where the plane-stress stiffness tensor has been non-dimensionalized on Young's modulus E. (See Appendix A for further details on the shell theory.) The non-dimensional load vector $\boldsymbol{f} = \boldsymbol{f}^*/K$ is given by

$$f_i = p_{ext} n_i + \left[-p n_i + \frac{1}{\alpha^2}\left(\frac{\partial u_i}{\partial x_j} + \frac{\partial u_j}{\partial x_i}\right) n_j\right]. \tag{4.4}$$

The non-dimensional form of the three-dimensional fluid–structure interaction problem is therefore given by equations (4.3) and (4.4) which must be solved simultaneously with the three-dimensional Navier–Stokes equations (3.3) in the domain bounded by (3.1), subject to the no-slip conditions (3.4).

The coupled system is governed by three main parameters: the ratio of the wall and fluid densities ρ_w/ρ_f, the Womersley number α, and the wall amplitude ϵ, the first two of which are material parameters. Large Womersley numbers correspond to cases with large wall stiffness and fluid density, and/or small fluid viscosity. Large Strouhal numbers correspond to cases in which the wall stiffness K is much larger than the inertial pressure, $\rho_f U^2$, associated with the steady through-flow. The assumptions $\alpha, St \gg 1$ underlying the analysis of § 3.1 can therefore be satisfied by making the wall sufficiently stiff. Under these conditions, the (predominantly transverse) unsteady flow and the associated unsteady fluid traction $\widehat{\boldsymbol{f}}$ on the wall of the three-dimensional tube can be determined independently in each of the tube's cross-sections.

4.2. *A two-dimensional fluid–structure interaction problem*

In this paper, we restrict ourselves to analysing the two-dimensional version of the fluid–structure interaction problem, by adding wall elasticity to the two-dimensional

https://doi.org/10.1017/S0022112005007214 Published online by Cambridge University Press

problem sketched in figure 1. To derive the equations that govern the wall deformation, we suppress the axial wall displacements and assume that $\boldsymbol{R}_w$ is independent of the axial Lagrangian coordinate ξ^1. The two-dimensional position vector to the deformed wall is then parameterized by the azimuthal Lagrangian coordinate $\zeta = \xi^2$ as

$$\boldsymbol{R}_w(\zeta, t) = \begin{pmatrix} \cos(\zeta) \\ \sin(\zeta) \end{pmatrix} + \epsilon \begin{pmatrix} \mathscr{V}(\zeta, t)\cos(\zeta) - \mathscr{U}(\zeta, t)\sin(\zeta) \\ \mathscr{V}(\zeta, t)\sin(\zeta) + \mathscr{U}(\zeta, t)\cos(\zeta) \end{pmatrix}, \tag{4.5}$$

where $\mathscr{U}(\zeta, t)$ and $\mathscr{V}(\zeta, t)$ are the scaled azimuthal and radial wall displacements to be determined from (4.3). In the two-dimensional problem, the external pressure, p_{ext}, and the steady fluid pressure, $\overline{p}$, are arbitrary constants and we set both to zero.

4.2.1. *Numerical simulations*

Numerical simulations of the fully coupled fluid–structure interaction problem were again performed with `oomph-lib`, using the fluid discretization already discussed in § 3.4.1. The one-dimensional version of the variational principle (4.3), which governs the deformation of the elastic wall, was discretized with cubic Hermite elements (Bogner, Fox & Schmit 1967). The BDF2 scheme and Newmark's method were employed to evaluate the time derivatives in the fluid and wall equations, respectively. The fluid and solid equations were solved with a 'monolithic' approach, using Newton's method to solve the system of nonlinear algebraic equations that arises from the coupled discretization.

a. Oscillations about non-axisymmetric equilibria

Figure 8 presents the results of numerical simulations for zero wall mass, $\rho_w/\rho_f = 0$, and for three different values of the Womersley number α. The wall deformation is characterized by the time evolution of the control radius $R_{ctrl}(t)$ identified in figure 1. All three simulations were started from an initial state in which the wall and the fluid are at rest and the wall is deformed by a displacement field of the form (3.18) with $\mathscr{A} = 1$, $N = 2$, $\mathbb{A} = -0.5$, and an amplitude of $\epsilon = 0.1$ so that $R_{ctrl}(t = 0) = 0.9$. At $t = 0$, the wall is 'released' and the system initially performs damped oscillations about its axisymmetric configuration, with velocity fields and wall shapes very similar to those described in § 3. The sketches in figure 9(*a*) illustrate the wall shapes that occur over one period of the oscillation; we shall refer to such oscillations as being of type I.

Figure 8 shows that the period of the oscillation is close to one, indicating that the time scale estimate of § 4.1 is appropriate, and confirming that the dynamics of the oscillation are indeed controlled by a balance between fluid inertia and wall elasticity. Since $\alpha \sim \mu^{-1/2}$, a reduction in Womersley number can be interpreted as an increase in fluid viscosity, explaining why the oscillations decay more rapidly for smaller α. In all three cases, the period of the oscillation increases slowly and at a certain point (indicated by the dashed vertical lines in figures 8(*b*) and 8(*c*)), the system suddenly switches to a different type of oscillation in which the wall performs oscillations about a non-axisymmetric configuration, as sketched in figure 9(*b*). We shall refer to these oscillations as being of type II.

To explain the mechanism responsible for the transition between the two types of oscillation we note that, because there is no external excitation, the system's total energy, Π_{total}, which comprises the strain energy and the kinetic energies of the wall and the fluid, decreases monotonically. The oscillations must therefore decay towards an equilibrium configuration in which the fluid and wall are both at rest. The inset in figure 8(*c*) shows that the ultimate equilibrium wall shape is non-axisymmetric. This

https://doi.org/10.1017/S0022112005007214 Published online by Cambridge University Press

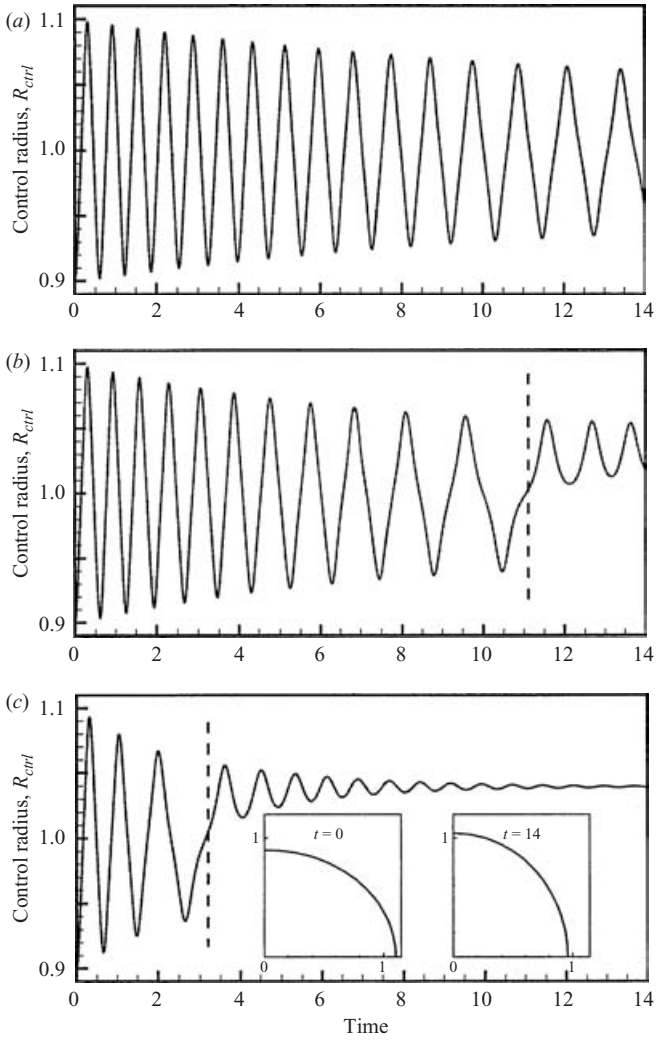


FIGURE 8. Time-trace of the control radius $R_{ctrl}(t)$ for oscillations with fluid–structure interaction for $\rho_w/\rho_f = 0$ and $h/a = 1/20$. Initially, the fluid and the wall are at rest and the initial wall displacement field is given by (3.18) with $N = 2$, $\mathbb{A} = -0.5$ and an amplitude of $\epsilon = 0.1$. (*a*) $\alpha^2 = 100$; (*b*) $\alpha^2 = 50$; (*c*) $\alpha^2 = 10$. The dashed vertical lines indicate the transition from type I to type II oscillations. The two insets in (*c*) show the initial and equilibrium wall shapes for $\alpha^2 = 10$.

is because the tube's cross-sectional area, $A_0 = A(t = 0)$, in the initial configuration (shown in the left-hand inset in figure 8*c*) is slightly less than the cross-sectional area A_{undef} in its undeformed circular state. As discussed in § 3.2, the change in cross-sectional area is only a second-order effect, $A_0 - A_{undef} = O(\epsilon^2)$, but the Navier–Stokes equations preserve the volume of fluid exactly. In the ultimate equilibrium configuration, shown in the right-hand inset in figure 8(*c*), the system satisfies the constraint $A = A_0$ by adopting a slightly buckled wall shape. We shall refer to this state as $\overline{\mathscr{B}^+}$. The system has two further equilibrium states in which $A = A_0$: a configuration $\overline{\mathscr{B}^-}$ in which the wall is buckled in the opposite direction to that shown in figure 8(*c*), and a configuration $\overline{\mathscr{A}}$ in which the tube wall is axisymmetric and

https://doi.org/10.1017/S0022112005007214 Published online by Cambridge University Press

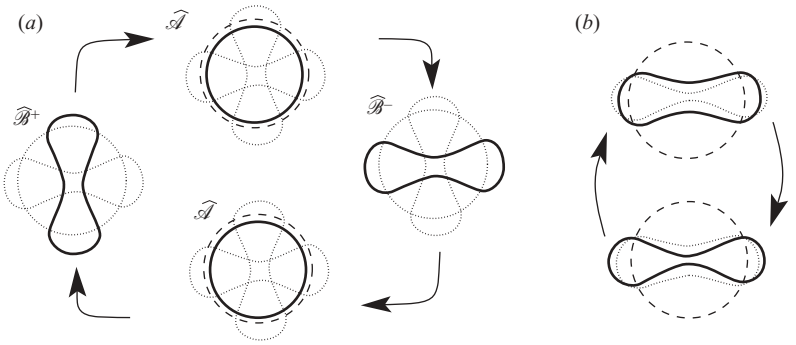


FIGURE 9. Sketch of the two types of oscillation. (*a*) Type I: the wall oscillates between two non-axisymmetric extremes, $\widehat{\mathscr{B}^+}$ and $\widehat{\mathscr{B}^-}$; the total energy in the system is sufficient to traverse the approximately axisymmetric state $\widehat{\mathscr{A}}$ in which the wall is compressed. (*b*) Type II: the wall performs small-amplitude oscillations about one of the system's two non-axisymmetric equilibrium states, $\overline{\mathscr{B}^+}$ or $\overline{\mathscr{B}^-}$. The long dashed lines represent the undeformed, stress-free wall shape. The wall displacements are exaggerated.

uniformly compressed. The wall's strain energy, Π_{strain} (defined in Appendix A) in state $\overline{\mathscr{A}}$ exceeds that in states $\overline{\mathscr{B}^+}$ and $\overline{\mathscr{B}^-}$, indicating that state $\overline{\mathscr{A}}$ is an unstable equilibrium.

The energy budget during the oscillation of figure 8(*c*) is illustrated in figure 10. The strain energy Π_{strain} has maxima whenever the wall reaches its extreme non-axisymmetric configurations, $\widehat{\mathscr{B}^+}$ and $\widehat{\mathscr{B}^-}$. At these instances, the fluid velocities (and hence Π_{kin}^{fluid}) are small and $\Pi_{strain} \approx \Pi_{total}$. Secondary maxima in Π_{strain} occur when the wall passes through the approximately axisymmetric configuration $\widehat{\mathscr{A}}$. During the early stages of the oscillation, $\Pi_{total} \gg \Pi_{strain}^{(\overline{\mathscr{A}})} \approx \Pi_{strain}^{(\widehat{\mathscr{A}})}$ and the potential-energy barrier associated with state $\widehat{\mathscr{A}}$ can be crossed with finite velocity, resulting in an oscillation similar to the one sketched in figure 9(*a*). As the oscillation proceeds, viscous dissipation continually reduces Π_{total} and the approximately axisymmetric state can no longer be traversed when $\Pi_{total} < \Pi_{strain}^{(\widehat{\mathscr{A}})}$. At this point, the oscillation ceases to be of type I and the system performs a damped oscillation about one of the two non-axisymmetric equilibrium states, as sketched in figure 9(*b*).

b. Oscillations about axisymmetric equilibria

The transition from a type I to a type II oscillation can only be avoided if the wall's initial cross-sectional area, $A(t = 0)$, is equal to its cross-sectional area, A_{undef}, in the undeformed stress-free configuration.

Figure 11 shows an example of such an oscillation. The fluid is initially at rest and the wall is in its undeformed configuration. The oscillation is initiated by applying the perturbation

$$\boldsymbol{f}_{trans} = \begin{cases} 10^{-6}\ \cos(N\zeta)\ \boldsymbol{n}_{\perp} & \text{for } t \leqslant 0.3, \\ \boldsymbol{0} & \text{for } t > 0.3, \end{cases} \tag{4.6}$$

to the load terms (4.4). This transient perturbation generates an oscillation with an initial amplitude of $\epsilon \approx 0.06$, which now decays slowly towards the axisymmetric equilibrium state. The period of the oscillation increases slowly from its initial value of $\mathscr{T} \approx 0.72$ and ultimately approaches a constant value of $\mathscr{T} \approx 1.44$. In this regime,

https://doi.org/10.1017/S0022112005007214 Published online by Cambridge University Press

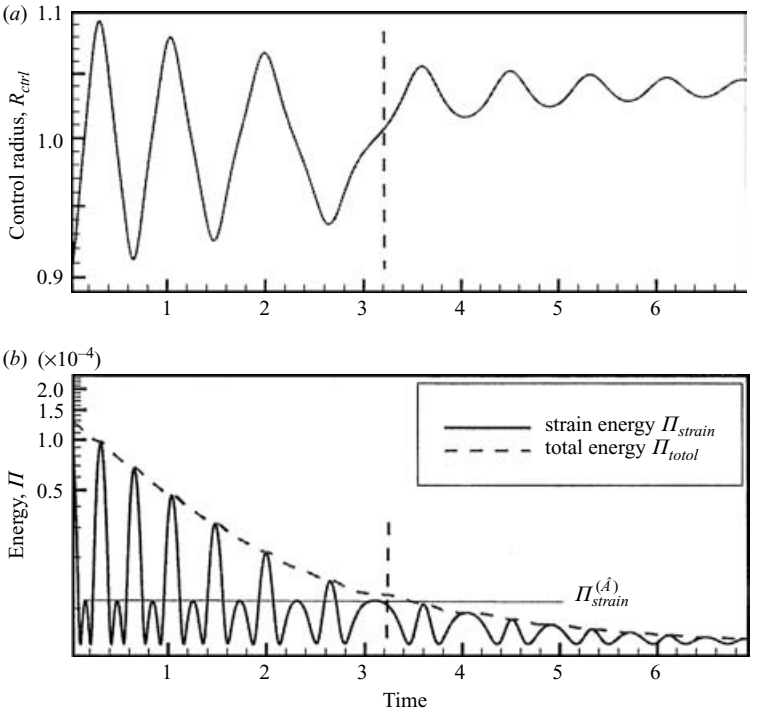


FIGURE 10. Illustration of the energy budget during the oscillation shown in figure 8(*c*). (*a*) The evolution of the control displacement; (*b*) the corresponding energies. The character of the oscillation changes when the system's total energy drops below the strain energy $\Pi^{(\hat{\mathscr{A}})}_{strain}$ required to traverse the approximately axisymmetric configuration.

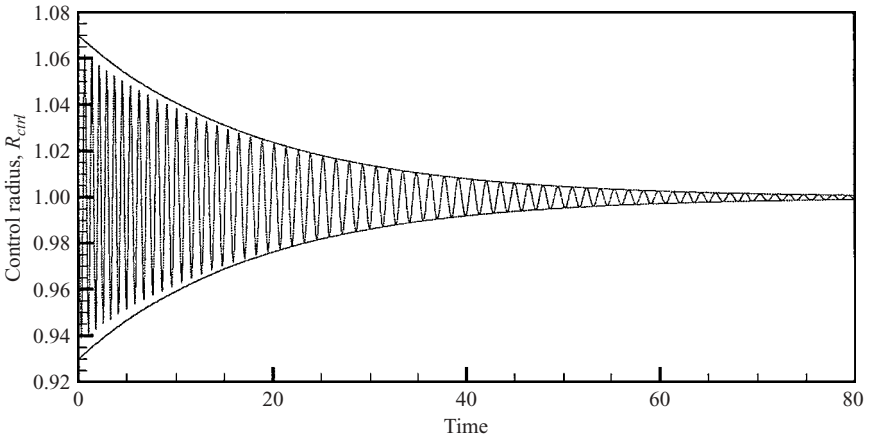


FIGURE 11. Time-trace of the control radius $R_{ctrl}(t)$ for oscillations with fluid–structure interaction and $\rho_w/\rho_f = 0$. Initially, the fluid and the wall are at rest and the oscillation is initiated by applying the short transient perturbation (4.6) to the traction that acts on the wall. As the amplitude of the oscillation decays, its period approaches a constant, $\mathscr{T} \approx 1.44$, and its amplitude decays exponentially, as shown by the two fitted envelopes $R^{(env)}_{ctrl} = 1 \pm 0.07 \exp(-kt)$ where $k = 0.054$. $\alpha^2 = 100$, $N = 2$, $h/a = 1/20$.

https://doi.org/10.1017/S0022112005007214 Published online by Cambridge University Press

the amplitude decreases exponentially, with a decay rate of $k \approx 0.054$, as shown by the two fitted envelopes in figure 11.

4.2.2. *Asymptotic analysis for small-amplitude coupled oscillations about axisymmetric equilibria*

We will now extend the analysis of § 3.4.2 to derive explicit predictions for the period and decay rate of small-amplitude coupled oscillations. At small amplitude, $\epsilon \ll 1$, and large Womersley number, $\alpha \gg 1$, the scalings of § 3.1 apply. Expanding the fluid velocity and the pressure at the wall (i.e. in the boundary layer) as in § 3.4.2 shows that the traction $\boldsymbol{f}$ that the fluid exerts on the wall has the form

$$\boldsymbol{f} = \epsilon(\widehat{\tau}_0\ \boldsymbol{e}_\zeta + \widehat{\mathscr{P}}_0\ \boldsymbol{e}_\rho) + O(\epsilon^2), \tag{4.7}$$

where

$$\widehat{\tau}_0 = \frac{1}{\alpha}\frac{\partial \widehat{U}^{\zeta}_{00}}{\partial n}\bigg|_{n=0} + O\left(\frac{1}{\alpha^2}\right) \tag{4.8}$$

and

$$\widehat{\mathscr{P}}_0 = \widehat{P}_{00}\bigg|_{n=0} + \frac{1}{\alpha}\widehat{P}_{01}\bigg|_{n=0} + O\left(\frac{1}{\alpha^2}\right). \tag{4.9}$$

We insert (4.5), (4.7), (4.8) and (4.9), and the expansion $(\mathscr{U}, \mathscr{V}) = (\mathscr{U}_0, \mathscr{V}_0) + \epsilon(\mathscr{U}_1, \mathscr{V}_1)\cdots$ into the Euler–Lagrange equations of the variational principle (4.3) and expand in powers of ϵ.

The leading-order equations for the wall displacements are given by

$$\frac{1}{12}\left(\frac{h}{a}\right)^3\left(\frac{\rho_w}{\rho_f}\right)\frac{\partial^2 \mathscr{U}_0}{\partial t^2} - \left(1 + \frac{1}{6}\left(\frac{h}{a}\right)^2\right)\frac{\partial \mathscr{V}_0}{\partial \zeta} + \frac{1}{6}\left(\frac{h}{a}\right)^2\frac{\partial^3 \mathscr{V}_0}{\partial \zeta^3} - \left(1 + \frac{1}{3}\left(\frac{h}{a}\right)^2\right)\frac{\partial^2 \mathscr{U}_0}{\partial \zeta^2} = \frac{1}{12}\left(\frac{h}{a}\right)^2\widehat{\tau}_0 \tag{4.10}$$

and

$$\frac{1}{12}\left(\frac{h}{a}\right)^3\left(\frac{\rho_w}{\rho_f}\right)\frac{\partial^2 \mathscr{V}_0}{\partial t^2} + \left(1 + \frac{1}{6}\left(\frac{h}{a}\right)^2\right)\frac{\partial \mathscr{U}_0}{\partial \zeta} + \left(1 + \frac{1}{12}\left(\frac{h}{a}\right)^2\right)\mathscr{V}_0 - \frac{1}{6}\left(\frac{h}{a}\right)^2\frac{\partial^2 \mathscr{V}_0}{\partial \zeta^2} - \frac{1}{6}\left(\frac{h}{a}\right)^2\frac{\partial^3 \mathscr{U}_0}{\partial \zeta^3} + \frac{1}{12}\left(\frac{h}{a}\right)^2\frac{\partial^4 \mathscr{V}_0}{\partial \zeta^4} = \frac{1}{12}\left(\frac{h}{a}\right)^2\widehat{\mathscr{P}}_0. \tag{4.11}$$

The numerical simulations show that the oscillations decay over a time scale that is much larger than the period of the oscillation. We exploit this by posing a multiple-scales expansion for all unknowns. For this purpose, we introduce a slow time scale $\mathfrak{T} = \alpha^{-1}t$ and write time derivatives as

$$\frac{\partial}{\partial t} \to \frac{\partial}{\partial t} + \frac{1}{\alpha}\frac{\partial}{\partial \mathfrak{T}}. \tag{4.12}$$

We now pose a normal mode expansion for the displacements

$$\begin{pmatrix}\mathscr{U}_0(\zeta, t, \mathfrak{T})\\ \mathscr{V}_0(\zeta, t, \mathfrak{T})\end{pmatrix} = \begin{pmatrix}\mathbb{U}\sin(N\zeta)\\ \mathbb{V}\cos(N\zeta)\end{pmatrix}\left(f_0(t, \mathfrak{T}) + \frac{1}{\alpha}f_1(t, \mathfrak{T}) + \cdots\right), \tag{4.13}$$

where

$$\mathbb{U} = \mathbb{U}_0 + \frac{1}{\alpha}\mathbb{U}_1 + \cdots,\ \ \mathbb{V} = \mathbb{V}_0 + \frac{1}{\alpha}\mathbb{V}_1 + \cdots, \tag{4.14}$$

https://doi.org/10.1017/S0022112005007214 Published online by Cambridge University Press

are the amplitudes of the azimuthal and radial wall displacements, respectively. For this wall shape, the components of the wall velocity relative to the $(\boldsymbol{e}_\rho, \boldsymbol{e}_\zeta)$ coordinate system, introduced in § 3.4.2, are given by

$$\widehat{U}_w^\rho(\zeta, t, \mathfrak{T}) = \cos(N\zeta)\left[\mathbb{V}_0\frac{\partial f_0}{\partial t} + \frac{1}{\alpha}\left(\mathbb{V}_0\left(\frac{\partial f_0}{\partial \mathfrak{T}} + \frac{\partial f_1}{\partial t}\right) + \mathbb{V}_1\frac{\partial f_0}{\partial t}\right) + \cdots\right], \quad (4.15)$$

$$\widehat{U}_w^\zeta(\zeta, t, \mathfrak{T}) = \sin(N\zeta)\left[\mathbb{U}_0\frac{\partial f_0}{\partial t} + \frac{1}{\alpha}\left(\mathbb{U}_0\left(\frac{\partial f_0}{\partial \mathfrak{T}} + \frac{\partial f_1}{\partial t}\right) + \mathbb{U}_1\frac{\partial f_0}{\partial t}\right) + \cdots\right]. \quad (4.16)$$

We expand the velocity and the pressure in powers of α^{-1} as in §3.4.2 and construct a perturbation solution for the coupled equations (3.11), (4.10) and (4.11).

a. The leading-order problem

The leading-order problem for $(\widehat{\boldsymbol{u}}_{00}, \widehat{p}_{00})$ is given by the inviscid equations (3.30) which must now be solved subject to

$$\widehat{u}_{00}^\rho(\rho = 1) = \mathbb{V}_0\frac{\partial f_0}{\partial t}\cos(N\zeta). \quad (4.17)$$

The solution is

$$\begin{pmatrix}\widehat{u}_{00}^\rho \\ \widehat{u}_{00}^\zeta\end{pmatrix} = \mathbb{V}_0\ \rho^{N-1}\ \frac{\partial f_0}{\partial t}\begin{pmatrix}\cos(N\zeta) \\ -\sin(N\zeta)\end{pmatrix}, \quad \widehat{p}_{00} = -\frac{\mathbb{V}_0}{N}\ \rho^N\ \frac{\partial^2 f_0}{\partial t^2}\cos(N\zeta). \quad (4.18)$$

As before, the velocity field (4.18*a*) does not satisfy the tangential component of the no-slip condition (4.16) and hence it is necessary to consider the flow in the Stokes layer. The leading-order equations which govern the flow in this layer are (3.32) with $\widehat{U}_w^\rho$ replaced by $\mathbb{V}_0\cos(N\zeta)\,\partial f_0/\partial t$. These equations must be solved subject to the no-slip conditions at $\rho = 0$

$$\widehat{U}_{00}^\rho = \left(\mathbb{V}_0\left(\frac{\partial f_0}{\partial \mathfrak{T}} + \frac{\partial f_1}{\partial t}\right) + \mathbb{V}_1\frac{\partial f_0}{\partial t}\right)\cos(N\zeta), \quad \widehat{U}_{00}^\zeta = \mathbb{U}_0\frac{\partial f_0}{\partial t}\sin(N\zeta) \quad (4.19)$$

and the leading-order matching conditions

$$\widehat{U}_{00}^\zeta \to -\mathbb{V}_0\frac{\partial f_0}{\partial t}\sin(N\zeta), \quad \widehat{P}_{00} \to -\frac{\mathbb{V}_0}{N}\frac{\partial^2 f_0}{\partial t^2}\cos(N\zeta) \quad \text{as} \quad n \to \infty. \quad (4.20)$$

The solution for $\widehat{P}_{00}$ is

$$\widehat{P}_{00} = -\frac{\mathbb{V}_0}{N}\frac{\partial^2 f_0}{\partial t^2}\cos(N\zeta), \quad (4.21)$$

therefore the leading-order terms in the wall equations (4.10) and (4.11) are given by

$$\mathscr{L}_1 f_0 = 0, \quad \mathscr{L}_2 f_0 = 0, \quad (4.22)$$

where $\mathscr{L}_1$ and $\mathscr{L}_2$ are the linear operators

$$\mathscr{L}_1 \equiv \frac{\mathbb{U}_0}{12}\left(\frac{h}{a}\right)^3\frac{\rho_w}{\rho_f}\frac{\partial^2}{\partial t^2} + \mathbb{V}_0\mathscr{F} + \mathbb{U}_0\mathscr{G}, \quad (4.23)$$

$$\mathscr{L}_2 \equiv \frac{\mathbb{V}_0}{12}\left(\frac{h}{a}\right)^2\left(\frac{h}{a}\frac{\rho_w}{\rho_f} + \frac{1}{N}\right)\frac{\partial^2}{\partial t^2} + \mathbb{V}_0\mathscr{H} + \mathbb{U}_0\mathscr{F}, \quad (4.24)$$

whose constant coefficients are given by

$$\mathscr{F} = \left(1 + \frac{1}{6}\left(\frac{h}{a}\right)^2(1 + N^2)\right)N, \quad (4.25)$$

https://doi.org/10.1017/S0022112005007214 Published online by Cambridge University Press

$$\mathscr{G} = \left(1 + \frac{1}{3}\left(\frac{h}{a}\right)^2\right) N^2, \tag{4.26}$$

$$\mathscr{H} = 1 + \frac{1}{12}\left(\frac{h}{a}\right)^2 (1 + N^2)^2. \tag{4.27}$$

This implies that $f_0(t, \mathfrak{T})$ has the form

$$f_0 = \mathfrak{A}(\mathfrak{T})\, \mathrm{e}^{\mathrm{i}\Omega t}, \tag{4.28}$$

where $\mathfrak{A}(\mathfrak{T})$ is a complex function of the slow time variable $\mathfrak{T}$. Inserting (4.28) into (4.23) and (4.24) yields

$$\boldsymbol{C}\boldsymbol{x} = \boldsymbol{0}, \tag{4.29}$$

where

$$\boldsymbol{C} = \begin{pmatrix} -\dfrac{\Omega^2}{12}\left(\dfrac{h}{a}\right)^3 \dfrac{\rho_w}{\rho_f} + \mathscr{G} & \mathscr{F} \\ \mathscr{F} & -\dfrac{\Omega^2}{12}\left(\dfrac{h}{a}\right)^2 \left(\dfrac{h}{a}\dfrac{\rho_w}{\rho_f} + \dfrac{1}{N}\right) + \mathscr{H} \end{pmatrix} \tag{4.30}$$

and $\boldsymbol{x} = (\mathbb{U}_0, \mathbb{V}_0)^T$. Non-trivial solutions of (4.29) exist only if $\det \boldsymbol{C} = 0$ and the characteristic polynomial

$$\frac{1}{12}\left(\frac{h}{a}\right)^2 \frac{\rho_w}{\rho_f}\left(\frac{h}{a}\frac{\rho_w}{\rho_f} + \frac{1}{N}\right)\Omega^4 - \left(\frac{h}{a}\frac{\rho_w}{\rho_f}\mathscr{H} + \left(\frac{h}{a}\frac{\rho_w}{\rho_f} + \frac{1}{N}\right)\mathscr{G}\right)\Omega^2 + N^2(1 - N^2)^2 = 0 \tag{4.31}$$

provides an equation for the eigenfrequency Ω. At finite wall mass, $\rho_w/\rho_f > 0$, the characteristic polynomial has two distinct roots Ω_1 and Ω_2, the larger of which (Ω_2) tends to infinity as $\rho_w/\rho_f \to 0$. The corresponding eigenvectors determine the ratio of the azimuthal and radial displacement components,

$$\mathbb{A}_i = \left(\frac{\mathbb{U}_0}{\mathbb{V}_0}\right)_i = \frac{-N\left(1 + \frac{1}{6}(h/a)^2(N^2+1)\right)}{\left(1 + \frac{1}{3}(h/a)^2\right)N^2 - \frac{1}{12}(h/a)^3(\rho_w/\rho_f)\Omega_i^2} \qquad \text{for } i = 1, 2. \tag{4.32}$$

Figure 12 illustrates the dependence of Ω_1 and Ω_2 on the density ratio ρ_w/ρ_f and contrasts the eigenfrequencies of fluid-filled rings with those of rings oscillating *in vacuo* (Soedel 1993; on the time scale $T = a\sqrt{\rho_f/K}$, the *in vacuo* frequencies obviously tend to infinity as $\rho_w/\rho_f \to 0$). Soedel's (1993) analysis of the *in vacuo* oscillations shows that the two eigenfrequencies are associated with two distinct modes of oscillation. In the low-(high-)frequency mode, the wall deformation is dominated by transverse bending (in-plane extensional) deflections. The frequencies are small (large) because the oscillations are governed by a balance between wall inertia and the wall's relatively small (large) bending (extensional) stiffness.

Figure 12 shows that at large wall mass, the oscillations are governed predominantly by a dynamic balance between wall inertia and wall stiffness – the 'added mass' due to the fluid loading causes only a small reduction in the frequencies. As the density ratio is reduced, fluid-inertia becomes more important and at $\rho_w/\rho_f = 0$, it provides the only form of inertia in the system. In this limit, only the low-frequency mode exists because, at leading order, the fluid loading does not have a component in the direction tangential to the wall (see (4.8)).

Figure 13 illustrates the dependence of the frequency Ω_1 on the wavenumber N. The frequency of the oscillation increases rapidly with N since (for a given amplitude

https://doi.org/10.1017/S0022112005007214 Published online by Cambridge University Press

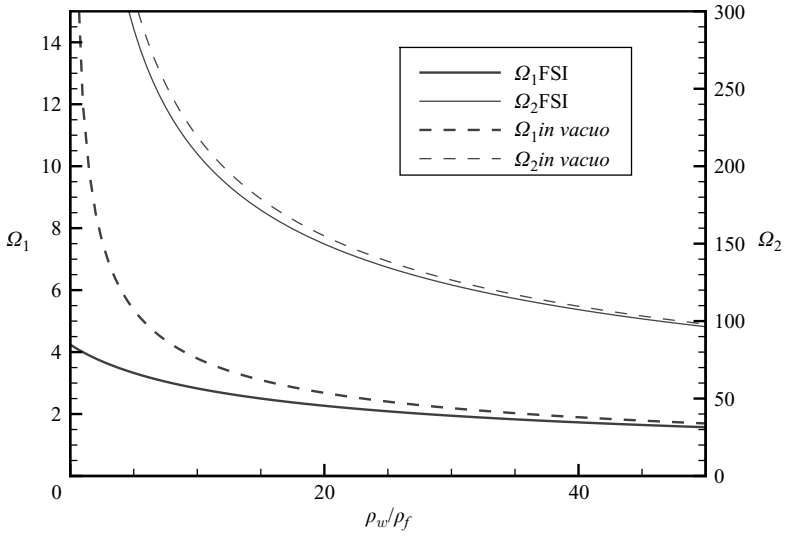


FIGURE 12. Eigenfrequencies of fluid-filled elastic rings as a function of the density ratio ρ_w/ρ_f for $N = 2$, $h/a = 1/20$. Ω_1 (thick lines) and Ω_2 (thin lines) correspond to modes that are dominated by bending and in-plane wall deformations, respectively. The dashed lines are Soedel's (1993) results for rings oscillating *in vacuo*.

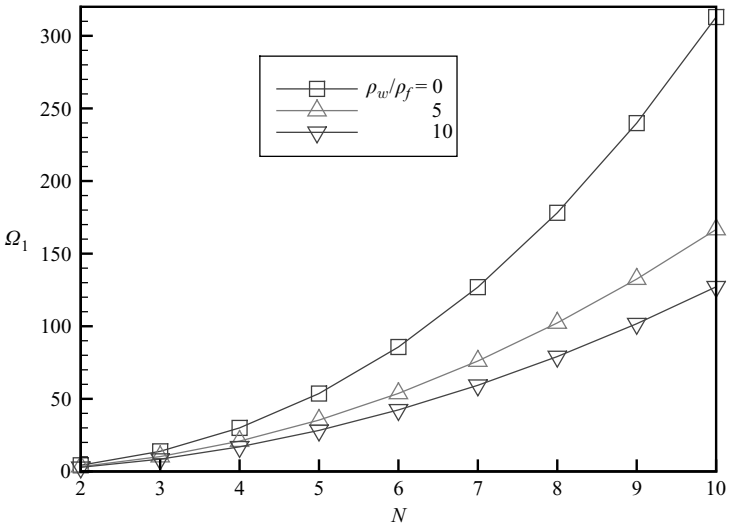


FIGURE 13. Eigenfrequency Ω_1 of the bending-dominated mode as a function of the azimuthal wavenumber N for various density ratios ρ_w/ρ_f. $h/a = 1/20$.

of the oscillation) wall deflections with shorter azimuthal wavelengths generate larger bending moments.

We note that for zero wall mass, $\rho_w/\rho_f = 0$, we have $\mathbb{A} = -1/N + O((h/a)^2)$. This shows that the amplitude ratio $\mathbb{A} = -0.5$ used in the numerical simulations of § 3.4.1 generates (prescribed) wall motions which resemble the eigenmodes of the fully coupled system.

With $f_0, \mathbb{U}_0$ and $\mathbb{V}_0$ available, the boundary and matching conditions (4.19) and (4.20) for the flow in the boundary layer are now fully specified, allowing us to solve

https://doi.org/10.1017/S0022112005007214 Published online by Cambridge University Press

for $\widehat{U}^{\zeta}_{00}$ and $\widehat{U}^{\rho}_{00}$, which are given by

$$\widehat{U}^{\zeta}_{00} = \mathrm{i}\ \Omega\ \mathfrak{A}(\mathfrak{T})\ \mathrm{e}^{\mathrm{i}\Omega t}\left[(\mathbb{U}_0+\mathbb{V}_0)\mathrm{e}^{-\sqrt{\Omega/2}(1+\mathrm{i})n}-\mathbb{V}_0\right]\sin(N\zeta), \tag{4.33}$$

$$\widehat{U}^{\rho}_{00} = \left[-N\sqrt{\tfrac{1}{2}\Omega}(1+\mathrm{i})(\mathbb{U}_0+\mathbb{V}_0)\mathfrak{A}(\mathfrak{T})\mathrm{e}^{\mathrm{i}\Omega t}\left(\mathrm{e}^{-\sqrt{\Omega/2}(1+\mathrm{i})n}-1\right)-\mathrm{i}\Omega(N-1)\mathbb{V}_0 n\mathfrak{A}(\mathfrak{T})\mathrm{e}^{\mathrm{i}\Omega t}\right.$$
$$\left.+\mathbb{V}_0\left(\frac{\partial\mathfrak{A}}{\partial\mathfrak{T}}\mathrm{e}^{\mathrm{i}\Omega t}+\frac{\partial f_1}{\partial t}\right)+\mathrm{i}\Omega\mathbb{V}_1\mathfrak{A}(\mathfrak{T})\mathrm{e}^{\mathrm{i}\Omega t}\right]\cos(N\zeta). \tag{4.34}$$

In order to determine $\mathfrak{A}(\mathfrak{T})$ we must proceed to the next order.

b. The first-order problem

At $O(\alpha^{-1})$ the governing equations in the core are

$$\frac{\partial\widehat{\boldsymbol{u}}_{01}}{\partial t}+\frac{\partial\widehat{\boldsymbol{u}}_{00}}{\partial\mathfrak{T}}=-\nabla_{\perp}\widehat{p}_{01},\quad \nabla_{\perp}\cdot\widehat{\boldsymbol{u}}_{01}=0, \tag{4.35}$$

which, from the matching condition (3.29*a*), must be solved subject to

$$\widehat{u}^{\rho}_{01}=\left[N\sqrt{\tfrac{1}{2}\Omega}(1+\mathrm{i})(\mathbb{U}_0+\mathbb{V}_0)\mathfrak{A}(\mathfrak{T})\mathrm{e}^{\mathrm{i}\Omega t}+\mathbb{V}_0\left(\frac{\partial\mathfrak{A}}{\partial\mathfrak{T}}\mathrm{e}^{\mathrm{i}\Omega t}+\frac{\partial f_1}{\partial t}\right)+\mathrm{i}\Omega\mathbb{V}_1\mathfrak{A}(\mathfrak{T})\mathrm{e}^{\mathrm{i}\Omega t}\right]\cos(N\zeta). \tag{4.36}$$

The solution is

$$\begin{pmatrix}\widehat{u}^{\rho}_{01}\\ \widehat{u}^{\zeta}_{01}\end{pmatrix}=\rho^{N-1}\left[N\sqrt{\tfrac{1}{2}\Omega}(1+\mathrm{i})(\mathbb{U}_0+\mathbb{V}_0)\mathfrak{A}(\mathfrak{T})\mathrm{e}^{\mathrm{i}\Omega t}+\mathbb{V}_0\left(\frac{\partial\mathfrak{A}}{\partial\mathfrak{T}}\mathrm{e}^{\mathrm{i}\Omega t}+\frac{\partial f_1}{\partial t}\right)\right.$$
$$\left.+i\Omega\mathbb{V}_1\mathfrak{A}(\mathfrak{T})\mathrm{e}^{\mathrm{i}\Omega t}\right]\begin{pmatrix}\cos(N\zeta)\\ -\sin(N\zeta)\end{pmatrix}, \tag{4.37}$$

$$\widehat{p}_{01}=-\frac{\rho^N}{N}\left[N\Omega\sqrt{\tfrac{1}{2}\Omega}\mathrm{i}(1+\mathrm{i})(\mathbb{U}_0+\mathbb{V}_0)\mathfrak{A}(\mathfrak{T})\mathrm{e}^{\mathrm{i}\Omega t}\right.$$
$$\left.+\mathbb{V}_0\left(2\mathrm{i}\Omega\frac{\partial\mathfrak{A}}{\partial\mathfrak{T}}\mathrm{e}^{\mathrm{i}\Omega t}+\frac{\partial^2 f_1}{\partial t^2}\right)-\Omega^2\mathbb{V}_1\mathfrak{A}(\mathfrak{T})\mathrm{e}^{\mathrm{i}\Omega t}\right]\cos(N\zeta). \tag{4.38}$$

The equation for the pressure in the boundary layer, $\widehat{P}_{01}$, is (3.36*b*) which must be solved subject to the matching condition

$$\widehat{P}_{01}\to-n\left.\frac{\partial\widehat{p}_{00}}{\partial\rho}\right|_1+\widehat{p}_{01}|_1\ \text{ as }\ n\to\infty. \tag{4.39}$$

The solution is

$$\widehat{P}_{01}=-\frac{1}{N}\left[N\Omega\sqrt{\tfrac{1}{2}\Omega}\mathrm{i}(1+\mathrm{i})(\mathbb{U}_0+\mathbb{V}_0)\mathfrak{A}(\mathfrak{T})\mathrm{e}^{\mathrm{i}\Omega t}+\mathbb{V}_0\left(2\mathrm{i}\Omega\frac{\partial\mathfrak{A}}{\partial\mathfrak{T}}\mathrm{e}^{\mathrm{i}\Omega t}+\frac{\partial^2 f_1}{\partial t^2}\right)\right.$$
$$\left.-\Omega^2(\mathbb{V}_1-\mathbb{V}_0 n)\mathfrak{A}(\mathfrak{T})\mathrm{e}^{\mathrm{i}\Omega t}\right]\cos(N\zeta). \tag{4.40}$$

We now consider the two wall equations, (4.10) and (4.11), at $O(\alpha^{-1})$. At this order, the tangential equation (4.10) is

$$\mathscr{L}_1 f_1=-\left[\frac{1}{12}\left(\frac{h}{a}\right)^2\left(\Omega\sqrt{\tfrac{1}{2}\Omega}\mathrm{i}(1+\mathrm{i})(\mathbb{U}_0+\mathbb{V}_0)+\frac{h}{a}\frac{\rho_w}{\rho_f}\right.\right.$$
$$\left.\left.\times\left(-\Omega^2\mathbb{U}_1+2\mathrm{i}\Omega\mathbb{U}_0\frac{1}{\mathfrak{A}(\mathfrak{T})}\frac{\partial\mathfrak{A}}{\partial\mathfrak{T}}\right)\right)+\mathbb{U}_1\mathscr{G}+\mathbb{V}_1\mathscr{F}\right]\mathfrak{A}(\mathfrak{T})\mathrm{e}^{\mathrm{i}\Omega t}, \tag{4.41}$$

https://doi.org/10.1017/S0022112005007214 Published online by Cambridge University Press

while the normal equation (4.11) is given by

$$\mathscr{L}_2 f_1 = -\left[\frac{1}{12}\left(\frac{h}{a}\right)^2\left(\Omega\sqrt{\tfrac{1}{2}\Omega}\,\mathrm{i}(1+\mathrm{i})(\mathbb{U}_0+\mathbb{V}_0)+\left(\frac{h}{a}\frac{\rho_w}{\rho_f}+\frac{1}{N}\right)\right.\right.$$
$$\left.\left.\times\left(-\Omega^2\mathbb{V}_1+2\mathrm{i}\Omega\mathbb{V}_0\frac{1}{\mathfrak{A}(\mathfrak{T})}\frac{\partial\mathfrak{A}}{\partial\mathfrak{T}}\right)\right)+\mathbb{V}_1\mathscr{H}+\mathbb{U}_1\mathscr{F}\right]\mathfrak{A}(\mathfrak{T})\mathrm{e}^{\mathrm{i}\Omega t}. \quad (4.42)$$

The secularity condition requires the terms in the square brackets on the right-hand sides of (4.41) and (4.42) to be identically zero. This implies

$$\boldsymbol{C}\boldsymbol{x}_1 = \boldsymbol{b}, \quad (4.43)$$

where $\boldsymbol{x}_1 = (\mathbb{U}_1, \mathbb{V}_1)^T$ and

$$\boldsymbol{b} = -\frac{1}{12}\left(\frac{h}{a}\right)^2\begin{pmatrix}\Omega\sqrt{\tfrac{1}{2}\Omega}\,\mathrm{i}(1+\mathrm{i})(\mathbb{U}_0+\mathbb{V}_0)+\dfrac{h}{a}\dfrac{\rho_w}{\rho_f}2\mathrm{i}\Omega\mathbb{U}_0\dfrac{1}{\mathfrak{A}}\dfrac{\partial\mathfrak{A}}{\partial\mathfrak{T}}\\ \Omega\sqrt{\tfrac{1}{2}\Omega}\,\mathrm{i}(1+\mathrm{i})(\mathbb{U}_0+\mathbb{V}_0)+\left(\dfrac{h}{a}\dfrac{\rho_w}{\rho_f}+\dfrac{1}{N}\right)2\mathrm{i}\Omega\mathbb{V}_0\dfrac{1}{\mathfrak{A}}\dfrac{\partial\mathfrak{A}}{\partial\mathfrak{T}}\end{pmatrix}. \quad (4.44)$$

Equation (4.43) must be evaluated for $\Omega = \Omega_i$ where $\Omega_i (i = 1, 2)$ are the eigenvalues determined from the leading-order analysis in § 4.2.2*a*. Since $\det \boldsymbol{C}(\Omega_i) = 0$, equation (4.43) has solutions if and only if

$$\boldsymbol{b}\cdot\boldsymbol{y} = 0, \quad (4.45)$$

where $\boldsymbol{y}$ is the solution of $\boldsymbol{C}^T\boldsymbol{y} = \boldsymbol{0}$. This solvability condition implies

$$\frac{1}{\mathfrak{A}}\frac{\partial\mathfrak{A}}{\partial\mathfrak{T}} = -\frac{1}{4}\frac{(1+\mathbb{A})^2(1+\mathrm{i})\sqrt{2\Omega}}{(h/a)(\rho_w/\rho_f)(1+\mathbb{A}^2)+1/N}. \quad (4.46)$$

Writing $\mathfrak{A}(\mathfrak{T}) = \mathscr{A}(\mathfrak{T})\mathrm{e}^{\mathrm{i}\Theta\mathfrak{T}}$ where $\mathscr{A}$ and Θ are real, we find, taking real and imaginary parts of (4.46), that the amplitude of the oscillations evolves according to

$$\frac{1}{\mathscr{A}}\frac{\partial\mathscr{A}}{\partial\mathfrak{T}} = -\frac{1}{4}\frac{(1+\mathbb{A})^2\sqrt{2\Omega}}{(h/a)(\rho_w/\rho_f)(1+\mathbb{A}^2)+1/N}. \quad (4.47)$$

Since $\mathfrak{T} = \alpha^{-1}t$, the amplitude decays like $\mathscr{A} \sim \exp(kt)$ where the decay rate k is given by

$$k = -\frac{1}{4\alpha}\frac{(1+\mathbb{A})^2\sqrt{2\Omega}}{(h/a)(\rho_w/\rho_f)(1+\mathbb{A}^2)+1/N}. \quad (4.48)$$

This shows that, since $k \sim \Omega^{1/2}$, the high-frequency oscillations associated with Ω_2 decay much more rapidly than the oscillations that are dominated by transverse deflections.

4.2.3. *Comparison between asymptotics and numerics*

To compare the asymptotic predictions for the period and decay rate of the oscillation against our numerical results, we performed a large number of numerical simulations for a wide range of Womersley numbers, $10 \leqslant \alpha^2 \leqslant 700$, and for cases with and without wall inertia. All simulations were started from the initial conditions described in § 4.2.1*b*. The transient perturbation (4.6) not only excites oscillations in the $N = 2$ bending mode, but also in a wide range of other modes. However, the $N = 2$ bending mode is dominant and also has the lowest possible frequency (see Figures 12

https://doi.org/10.1017/S0022112005007214 Published online by Cambridge University Press

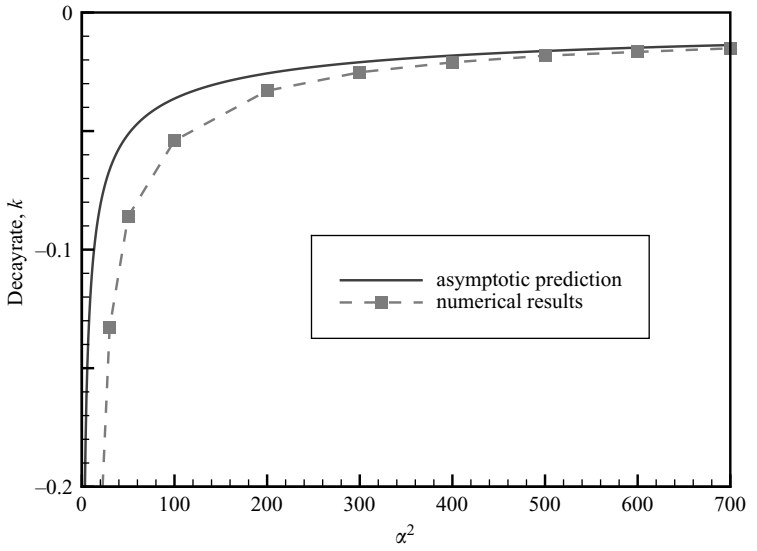


FIGURE 14. The decay rate, k, of the oscillations as a function of the Womersley number α^2, for $\rho_w/\rho_f = 0$. The solid line represents the asymptotic prediction (4.48); markers, connected by the straight dashed lines, represent the results from the numerical simulations. $N = 2$, $h/a = 1/20$.

and 13). Therefore, the other modes decayed much more quickly and soon became negligible.

The simulations confirmed the period of small-amplitude oscillations to be approximately independent of α and confirmed the predictions (4.31) for the dependence of Ω on the density ratio ρ_w/ρ_f. For instance, for $N = 2$, $h/a = 1/20$ and $\rho_w/\rho_f = 0$, the oscillations approached a period of $\mathscr{T} \approx 1.44$ as the amplitude decayed. This differs by less than 3 % from the theoretical prediction $\mathscr{T} \approx 1.48$. To determine the decay rate of the oscillation, we plotted the natural logarithm of $|R_{ctrl}(t) - 1|$ as a function of time. The plots confirmed that small-amplitude oscillations decay exponentially towards the axisymmetric equilibrium state and allowed the decay rate to be determined from the slope of the graph's envelope. Figure 14 shows a comparison of the decay rates with the theoretical predictions from (4.48). The theoretical predictions systematically underestimate the decay rate, but the error decreases rapidly with increasing Womersley number.

5. Summary and further discussion

We have analysed high-frequency oscillations of fluid-conveying elastic tubes and shown that, for sufficiently small amplitudes, the three-dimensional unsteady flow induced by the wall motion is independent of the steady through-flow. Furthermore, the average axial velocities that are generated by the wall motion are much smaller than the corresponding transverse velocities, suggesting that the dominant flow occurs in the tube's transverse cross-sections. This is an important difference to the two-dimensional case considered by Jensen & Heil (2003), where high-frequency wall oscillations drive axial 'sloshing' flows which play an important role in the development of the instability analysed in their study.

https://doi.org/10.1017/S0022112005007214 Published online by Cambridge University Press

We used numerical simulations and asymptotic methods to analyse the structure of the two-dimensional transverse flows that develop in the tube's cross-sections at large Strouhal and Womersley numbers. The velocity field was shown to consist of an unsteady stagnation point flow in the core, matched to the walls by thin Stokes layers. In cases with fluid–structure interaction, a dynamic balance between fluid inertia and wall stiffness can support oscillations of the type assumed in the theoretical analysis, provided the wall stiffness is sufficiently large. Numerical simulations of the coupled oscillations in a two-dimensional model system (a fluid-filled elastic ring) showed that the character of the oscillations depends strongly on the ring's initial cross-sectional area A_0. If A_0 is equal to the ring's cross-sectional area A_{undef} in the undeformed stress-free configuration, the wall performs damped harmonic oscillations about the axisymmetric equilibrium state. The frequency and decay rate of these oscillations were predicted accurately by a multiple-scales analysis. In cases where the oscillations are started from a configuration in which the ring's cross-sectional area is less than A_{undef}, the system's evolution has two distinct phases. During the early stages of the oscillation, the wall oscillates symmetrically about its axisymmetric configuration – a type I oscillation. As the amplitude decays, the character of the oscillation changes and ultimately the wall performs small-amplitude oscillations about one of its two non-axisymmetric equilibrium configurations – a type II oscillation.

We wish to stress that the transition from a type I to a type II oscillation is not merely an artifact of the two-dimensional model problem but is, in fact, a feature that is commonly observed in collapsible tube oscillations. The analysis of § 4.2.1*a* showed that the transition from a type I to a type II oscillation is caused by the static instability of the axisymmetric equilibrium state $\overline{\mathscr{A}}$. In collapsible-tube experiments, large-amplitude self-excited oscillations arise predominantly in situations in which the external pressure is so large that, in the absence of through-flow, the tube buckles non-axisymmetrically, indicating that the axisymmetric configuration is unstable. Hence, the distribution of equilibrium states is completely analogous to the one found here: an unstable axisymmetric equilibrium is surrounded by two topologically equivalent, stable non-axisymmetric states. In many experiments it is found that under these conditions, the tubes readily perform large-amplitude oscillations 'with the antinodes snapping through alternately between the positive and negative extremes of the modal form involved' (Paidoussis & Li 1993) – a type I oscillation. When such oscillations decay, they must eventually change to oscillations of type II when the wall approaches its non-axisymmetric equilibrium shape, just as in the simulations shown in figure 8.

Conversely, small-amplitude oscillations that arise from a linear instability of steady flow in non-axisymmetrically buckled tubes will initially have to be of type II because the wall will oscillate about its (temporally unstable) non-axisymmetric equilibrium state. A 'reversed' version of the transition shown in figure 8 is then required before the system can settle into the large-amplitude type I oscillations that are observed experimentally.

The scaling analysis of § 4.1 shows that the parameter regime considered in our study ($\epsilon \ll 1$, $St \gg 1$ and $\alpha \gg 1$) can be realized experimentally by making the wall sufficiently stiff. To assess the significance of our results for existing collapsible tube experiments, we derive estimates of the relevant non-dimensional parameters for experiments that have been reported in the literature. Collapsible tubes are typically made of rubber ($E \approx 1.1 \times 10^6$ Pa, $\nu \approx 0.5$). We consider the collapsible tubes used in Heil's (1997) experiments ($a = 4.2 \times 10^{-3}$ m, $h/a = 0.1$) as a representative example for thin-walled tubes. If water ($\rho_f = 1000\,\mathrm{kg\,m^{-3}}$, $\mu = 1.0 \times 10^{-3}\,\mathrm{kg\,m^{-1}\,s^{-1}}$)) is used as the working fluid, equation (4.1) yields a Womersley number of $\alpha^2 = 1460$.

https://doi.org/10.1017/S0022112005007214 Published online by Cambridge University Press

For the relatively thick-walled tubes used in Bertram, Raymond & Pedley's (1990) experiments ($a = 6.5 \times 10^{-3}$ m, $h/a = 0.3$), we obtain $\alpha^2 = 11\,730$, indicating that the assumption $\alpha \gg 1$ generally tends to be satisfied. The Strouhal numbers in most collapsible-tube oscillations tend to be moderate, however, and even for the high-frequency oscillations reported in figure 2 of Bertram *et al.* (1990), equation (4.2) only yields $St = 1.33$ for a flow rate of $Q = UA^* = 180 \times 10^{-6}\,\mathrm{m^3\,s^{-1}}$. Similar values are obtained directly from the definition of $St = a/(U\mathscr{T}^*)$ using the reported period of the oscillation. Although this is clearly not large enough to formally justify the large Strouhal-number assumption underlying the analysis in this paper, Jensen & Heil (2003) found that their large Strouhal-number theory worked perfectly at $St = 0.5$ and still captured the essential physics of the flow at $St = 0.05$.

The scaling arguments of § 3.1 show that the leading-order oscillatory flow, $\widehat{\boldsymbol{u}}_0$, that is driven by small-amplitude high-frequency wall oscillations is independent of the steady through flow $\overline{\boldsymbol{u}}$. Consequently, at small amplitudes, the oscillations do not interact with the mean flow and can therefore not extract any energy from it. This implies that, at least in the parameter regime considered here, viscous dissipation will always cause small-amplitude oscillations to decay. Self-excited oscillations can therefore develop only if the amplitude of the wall oscillation becomes large enough for nonlinear effects to become important. Such nonlinear effects will first manifest themselves in the velocity perturbation $\widehat{\boldsymbol{u}}_1$ whose axial component $\widehat{w}_1$ will have a non-zero cross-sectional average. At this order, we will therefore recover the axial 'sloshing' flows that played such a crucial role in the two-dimensional instability mechanism analysed by Jensen & Heil (2003). The explicit predictions for the viscous dissipation derived in § 3.4.2 of this paper provide lower bounds for the amount of energy that the interaction with the mean flow must generate before oscillations can grow in amplitude.

The authors wish to thank the referees for their helpful comments which led to significant improvements of the original manuscript. M. H. wishes to acknowledge many helpful and enjoyable discussions with Dr Andrew Hazel, and financial support from the EPSRC for an Advanced Research Fellowship. This study was initiated during M. H.'s four-months visit to LadHyX in 2003 and it is a pleasure to thank Professor Emmanuel de Langre and his colleagues for their hospitality. S. L. W. gratefully acknowledges a Discipline Hopping Award from the MRC.

Appendix A. Further details of the shell theory

The derivation of the two-dimensional strain and bending tensors $\gamma_{\alpha\beta}$ and $\gamma_{\alpha\beta}$ and the stiffness tensor $E^{\alpha\beta\gamma\delta}$ may be found in Appendix A of Hazel & Heil (2003). For the axially uniform deformations considered in § 4.2 of the present paper, the only non-zero components of these tensors are

$$E^{2222} = \frac{1}{1-\nu^2}, \tag{A 1}$$

where ν is Poisson's ratio, and

$$\gamma_{22} = \frac{1}{2}\left(\frac{\partial \boldsymbol{R}_w}{d\zeta}\cdot\frac{\partial \boldsymbol{R}_w}{d\zeta} - 1\right), \quad \kappa_{22} = -\left(1 - \boldsymbol{n}\cdot\frac{\partial^2 \boldsymbol{R}_w}{d\zeta^2}\right). \tag{A 2}$$

https://doi.org/10.1017/S0022112005007214 Published online by Cambridge University Press

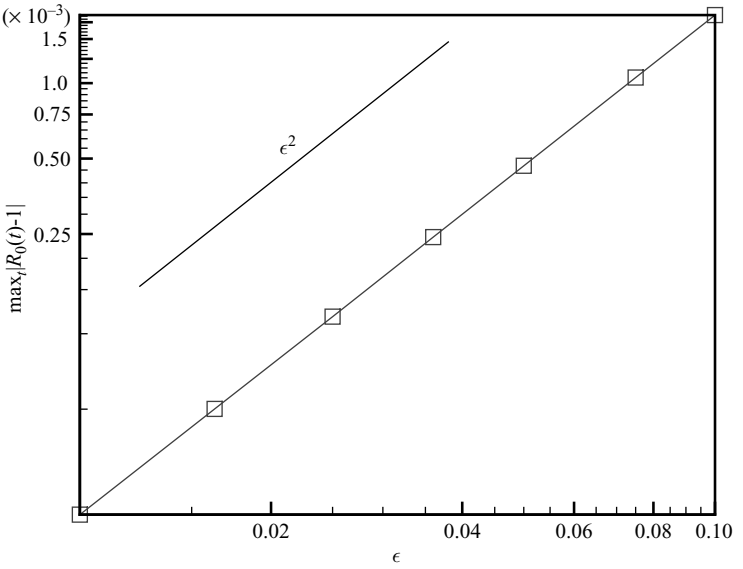


FIGURE 15. Maximum deviation of the 'mean radius' $R_0(t)$ from $R_0 = 1$ as a function of the wall amplitude ϵ, for the prescribed wall motion given by (3.18) with $N = 2$. The markers represent computational results.

Here, $\boldsymbol{n}$ is the inner unit normal on the deformed ring and $\boldsymbol{R}_w(\zeta)$ is given by (4.5). The non-dimensional strain energy stored in the deformed wall is given by

$$\Pi_{strain} = \frac{\Pi^*_{strain}}{haE/(1-\nu^2)} = \frac{1}{2}\int_0^{2\pi} \left(\gamma_{22}\gamma_{22} + \frac{1}{12}\left(\frac{h}{a}\right)^2 \kappa_{22}\kappa_{22}\right) \mathrm{d}\zeta. \tag{A 3}$$

Appendix B. The change in the mean radius $R_0(t)$ is a second-order effect

In § 3.2, we showed that the change in the cross-sectional area induced by the displacement field (3.17) is an $O(\epsilon^2)$ effect and can therefore be neglected in our asymptotic analysis. Nevertheless, the displacement field violates the exact mass conservation required by the Navier–Stokes equations (3.3) which formed the basis for our numerical simulations. In the computations we therefore treated the mean radius R_0 as a variable and determined its value as part of the solution, allowing mass to be conserved exactly. Figure 15 shows a plot of $\max_{t\in[0,1]} |R_0(t) - 1|$ as a function of the displacement amplitude ϵ. The plot demonstrates that the maximum deviation of the mean radius from unity is very small and that the deviation scales with ϵ^2, as predicted by the analysis.

Appendix C. Symmetry of the flow

Throughout this study we have assumed the flow and the wall deformation to be periodic in the azimuthal direction. This simplified the analysis and allowed us to perform the numerical simulations for the $N = 2$ case in a quarter of the domain. However, symmetry-breaking bifurcations are common in high-Reynolds-number flows and Kouanis & Mathioulakis (1999) have observed symmetry breaking in three-dimensional collapsible-tube experiments.

We have not formally investigated the stability of our symmetric solutions, but note that Hall & Papageorgiou (1999) have considered the two-dimensional flow

https://doi.org/10.1017/S0022112005007214 Published online by Cambridge University Press

between parallel walls, driven by time-periodic oscillation of one of the walls. The flow is a Navier–Stokes solution of the stagnation-point type and so has similarities to the unsteady stagnation-point flow we find here. The flow is characterized by a dimensionless amplitude (corresponding to our ϵ) and an unsteady Reynolds number (corresponding to our α^2). In the small-amplitude limit, Hall & Papageorgiou's results predict the flow to be stable for values of α^2 less than $O(1/\epsilon^2)$. This is equivalent to $\epsilon \ll 1/\alpha$ which is one of our asymptotic requirements. Thus we expect our stagnation-point flow to remain stable.

REFERENCES

Bertram, C. D. 2003 Experimental studies of collapsible tubes. In *Flow in Collapsible Tubes and Past Other Highly Compliant Boundaries* (ed. T. J. Pedley & P. W. Carpenter), pp. 51–65. Kluwer.

Bertram, C. D., Raymond, C. J. & Pedley, T. J. 1990 Mapping of instabilities for flow through collapsible tubes of differering length. *J. Fluids Struct.* **4**, 125–153.

Bogner, F. K., Fox, R. L. & Schmit, L. A. 1967 A cylindrical shell discrete element. *AIAA J.* **5**, 645–750.

Hall, P. & Papageorgiou, D. J. 1999 The onset of chaos in a class of Navier–Stokes solutions. *J. Fluid Mech.* **393**, 59–87.

Hazel, A. L. & Heil, M. 2003 Steady finite Reynolds number flow in three-dimensional collapsible tubes. *J. Fluid Mech.* **486**, 79–103.

Heil, M. 1997 Stokes flow in collapsible tubes: computation and experiment. *J. Fluid Mech.* **353**, 285–312.

Heil, M. & Hazel, A. L. 2005 `oomph-lib`: the object-oriented multi-physics finite-element library. `http://www.oomph-lib.org/`.

Heil, M. & Jensen, O. E. 2003 Flows in deformable tubes and channels – theoretical models and biological applications. In *Flow in Collapsible Tubes and Past Other Highly Compliant Boundaries* (ed. T. J. Pedley & P. W. Carpenter), pp. 15–50. Kluwer.

Hinch, E. J. 1991 *Perturbation Methods*. Cambridge University Press.

HSL 2000 A collection of Fortran codes for large scale scientific computation. http://www.numerical.rl.ac.uk. (Now available as HSL 2004 at http://www.cse.clrc.ac.uk/nag/hsl/).

Jensen, O. E. & Heil, M. 2003 High-frequency self-excited oscillations in a collapsible-channel flow. *J. Fluid Mech.* **481**, 235–268.

Kouanis, K. & Mathioulakis, D. S. 1999 Experimental flow study within a self oscillating collapsible tube. *J. Fluids Struct.* **13**, 61–73.

Paidoussis, M. P. & Li, G. X. 1993 Pipes conveying fluid: a model dynamical problem. *J. Fluids Struct.* **7**, 137–204.

Soedel, W. 1993 *Vibrations of Shells and Plates*. Marcel Dekker.

van Dyke, M. 1964 *Perturbation Methods in Fluid Mechanics*. Academic.

Wempner, G. A. 1981 *Mechanics of Solids with Applications to Thin Bodies*. Sijthoff & Noordhoff, Alphen aan den Rijn.

Zienkiewicz, O. C. & Zhu, J. Z. 1992 The superconvergent patch recovery and a posteriori error estimates. Part 1: The recovery technique. *Intl J. Numer. Meth. Engng* **33**, 1331–1364.

https://doi.org/10.1017/S0022112005007214 Published online by Cambridge University Press